ACS OMEGA

http://pubs.acs.org/journal/acsodf

Article

Nonconventional NMR Spin-Coupling Constants in Oligosaccharide Conformational Modeling: Structural Dependencies Determined from Density Functional Theory Calculations

Reagan J. Meredith, Ian Carmichael, and Anthony S. Serianni*

Cite This: *ACS Omega* 2022, 7, 23950−23966

Read Online

ACCESS | Metrics & More | Article Recommendations | Supporting Information

ABSTRACT: Nonconventional NMR spin-coupling constants were investigated to determine their potential as conformational constraints in *MA'AT* modeling of the *O*-glycosidic linkages of oligosaccharides. Four ($^{1}J_{C1',H1'}$, $^{1}J_{C1',C2'}$, $^{2}J_{C1',H2'}$, and $^{2}J_{C2',H1'}$) and eight ($^{1}J_{C4,H4}$, $^{1}J_{C3,C4}$, $^{1}J_{C4,C5}$, $^{2}J_{C3,H4}$, $^{2}J_{C4,H3}$, $^{2}J_{C5,H4}$, $^{2}J_{C4,H5}$, and $^{2}J_{C3,C5}$) spin-couplings in methyl β-D-galactopyranosyl-(1→4)-β-D-glucopyranoside (methyl β-lactoside) were calculated using density functional theory (DFT) to determine their dependencies on *O*-glycosidic linkage C−O torsion angles, ϕ and ψ, respectively. Long-range $^{4}J_{H1',H4}$ was also examined as a potential conformational constraint of either ϕ or ψ. Secondary effects of exocyclic (hydroxyl) C−O bond rotation within or proximal to these coupling pathways were investigated. Based on the findings of methyl β-lactoside, analogous *J*-couplings were studied in five additional two-bond *O*-glycosidic linkages [βGlcNAc-(1→4)-βMan, 2-deoxy-βGlc-(1→4)-βGlc, αMan-(1→3)-βMan, αMan-(1→2)-αMan, and βGlcNAc(1→2)-αMan] to determine whether the coupling behaviors observed in methyl β-lactoside were more broadly observed. Of the 13 nonconventional *J*-couplings studied, 7 exhibit properties that may be useful in future *MA'AT* modeling of *O*-glycosidic linkages, none of which involve coupling pathways that include the linkage C−O bonds. The findings also provide new insights into the general effects of exocyclic C−O bond conformation on the magnitude of experimental spin-couplings in saccharides and other hydroxyl-containing molecules.

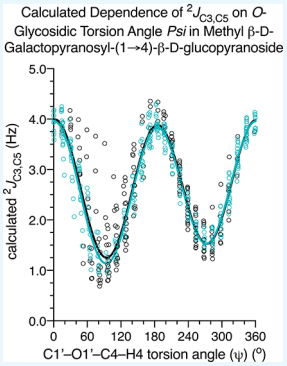

1. INTRODUCTION

Determinations of oligosaccharide structure in solution require, in part, assessments of the geometries of their constituent *O*-glycosidic linkages.[1−3] Theoretical methods such as aqueous molecular dynamics (MD) simulations[4−8] can provide this information if their underlying force fields are parameterized to accurately and quantitatively recapitulate all of the covalent and non-covalent interactions that dictate geometry in solution. Conformational models obtained by MD simulations are only as reliable as the force field that underpins them. However, it has been difficult to obtain rigorous independent experimental validation of MD-derived models because current experimental methods do not provide continuous models of molecular torsion angles that can be superimposed on those obtained by MD. Recent developments using redundant experimental NMR spin-coupling constants and *MA'AT* analysis[9−12] offer a solution to this problem. *MA'AT* analysis allows the testing of uni- and multi-modal conformational models, but a significantly greater number of experimental observables is required to test the latter. For example, rotational models about the C5−C6 bond in methyl β-D-glucopyranoside (**1**) typically involve three states, each representing an idealized staggered rotamer of the C4−C5−C6−O6 torsion angle ω (Scheme 1). Testing this model of ω using *MA'AT* analysis requires at least 7 redundant spin-

Scheme 1. Conformational Model of the C4−C5−C6−O6 Torsion Angle in Methyl β-D-Glucopyranoside (1) in Solution, Comprising Three Idealized Staggered Rotamers *gg*, *gt*, and *tg* in Chemical Exchange

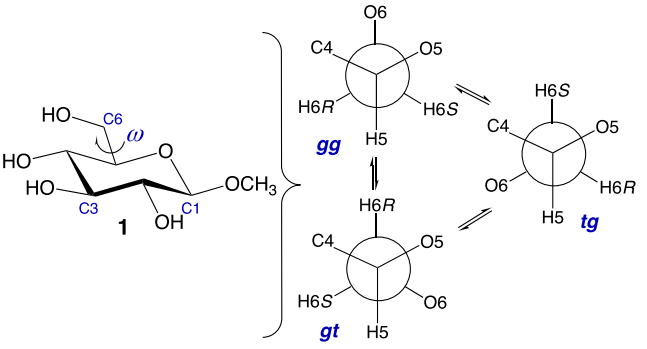

Received: May 5, 2022
Accepted: June 13, 2022
Published: July 1, 2022

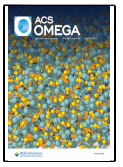

coupling constants, and, in this case, >12 are available,[13] rendering the treatment feasible mathematically.

Conventional modeling of *O*-glycosidic linkages using *MA'AT* analysis typically employs six trans-*O*-glycosidic *J*-couplings to characterize ϕ and ψ, which includes three redundant couplings to model ϕ and three to model ψ (Scheme 2).[14] Recent work has shown that these six *J*-values

Scheme 2. Conventional Trans-*O*-Glycosidic *J*-coupling Pathways in β-(1→4) Disaccharide 2, Showing Three *J*-Couplings Sensitive to φ ($^3J_{H1',C4}$, $^2J_{C1',C4}$, and $^3J_{C2',C4}$) and Three Sensitive to ψ ($^3J_{C1',H4}$, $^3J_{C1',C3}$, and $^3J_{C1',C5}$)[a]

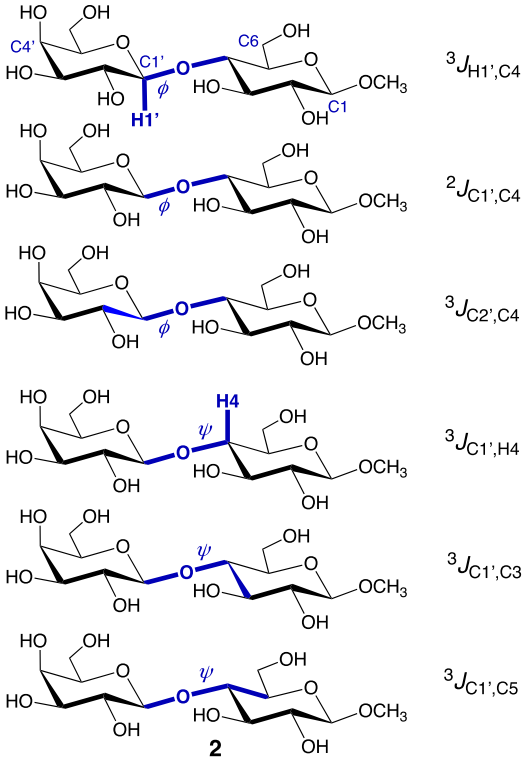

[a]Atom numbering and glycosidic torsion angles φ and ψ are shown. Coupling pathways are highlighted in blue.

associated with C−O−C−H, C−O−C−C, and C−O−C coupling pathways across *O*-glycosidic linkages are sufficient for unimodal modeling of each torsion angle.[10−12,15] These treatments yield mean torsion angles and circular standard deviations that are in good agreement with other techniques, the latter reporting on the degree of librational motion of each angle. Determinations of root mean squared deviations (RMSDs) of these models and inspections of parameter space plots yield information on how well unimodal models fit the available experimental *J*-couplings and whether the model is a unique fit of the experimental data, respectively. In the linkages studied to date, RMSDs are small (<0.3 Hz), and the majority produce unique fits, indicating that ϕ and ψ adopt highly preferred single states, although considerable averaging around the mean torsion angles is observed. *MA'AT* modeling of ϕ in different types of *O*-glycosidic linkages suggests that current MD models underestimate the librational motion about this glycosidic torsion angle.[15] Despite these advances, however, it would be desirable to increase the number of redundant spin-coupling constants used in *MA'AT* analyses of linkage conformation (or include other types of NMR constraints) to test unimodal models more rigorously and/or to render feasible modeling beyond a single state.

The results of the studies described herein address the structural dependences of several nonconventional NMR spin-coupling constants that may serve as potential constraints in *MA'AT* analyses of *O*-glycosidic linkages. The primary objective of the work was to determine which of these *J*-couplings have properties conducive to their use in *MA'AT* analysis. The structural dependencies were determined by density functional theory (DFT) calculations in four different types of linkages (α-(1→2); β-(1→2); α-(1→3); and β-(1→4); Scheme 3) found in disaccharides **2**−**7** to determine the

Scheme 3. Chemical Structures of Methyl β-D-Galactopyranosyl-(1→4)-β-D-glucopyranoside (2), Methyl 2-Acetamido-2-deoxy-β-D-glucopyranosyl-(1→4)-β-D-mannopyranoside (3), Methyl 2-Deoxy-β-D-arabino-hexopyranosyl-(1→4)-β-D-glucopyranoside(4), Methyl α-D-mannopyranosyl-(1→3)-β-D-mannopyranoside (5), Methyl α-D-mannopyranosyl-(1→2)-α-D-mannopyranoside (6), and Methyl 2-Acetamido-2-deoxy-β-D-glucopyranosyl-(1→2)-α-D-mannopyranoside (7), Showing Atom Numbering in the Pyranosyl Rings and Identification of the "a" and "b" Residues of Each Disaccharide[a]

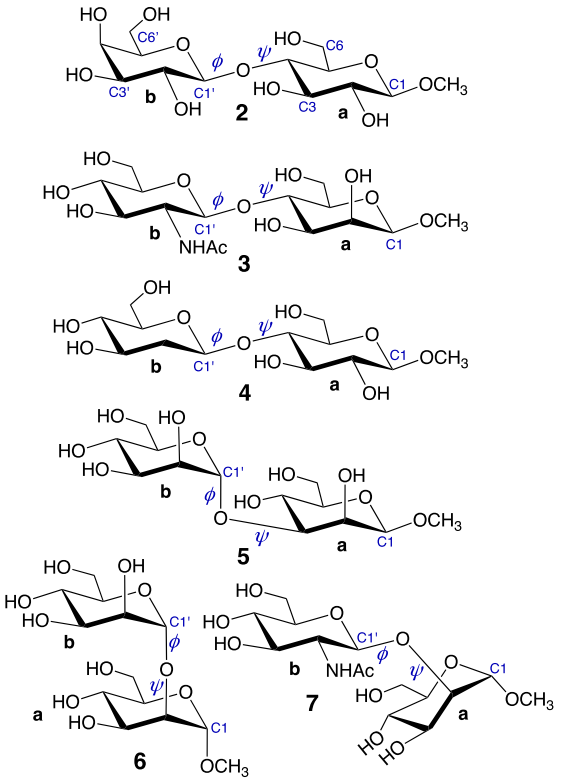

[a]The *O*-glycosidic torsion angles phi (φ) and psi (ψ) are shown in each structure.

extent to which the results are generalizable. We show that several coupling pathways, some of which are peripheral to the linkages themselves and do not include linkage bonds explicitly, yield *J*-couplings that may prove useful in future *MA'AT* treatments of *O*-glycosidic linkages. This work also reveals the importance of understanding the conformational behaviors of exocyclic C−O bonds of saccharides in solution since they impact the values and structural interpretations of

https://doi.org/10.1021/acsomega.2c02793
ACS Omega 2022, 7, 23950−23966

both conventional and nonconventional experimental *J*-couplings.

2. CALCULATIONS

2.1. Geometry Optimizations. DFT calculations were conducted on fully substituted model structures **2**−**7** (Scheme 3) within *Gaussian*09[16] using the B3LYP functional[17,18] and the 6-31G* basis set.[19] In models **5** and **7**, several sites of deoxygenation were introduced at carbons remote from the coupling pathways of interest (Schemes S6 and S8, Supporting Information; see explanation below). In all geometric optimizations, the effects of solvent water were treated using the self-consistent reaction field (SCRF)[20] and the integral equation formalism (polarizable continuum) model (IEFPCM).[21] For calculations on **2**, the phi (ϕ) and psi (ψ) *O*-glycosidic torsion angles, defined as O5′−C1′−O1′−C4 and C1′−O1′−C4−C3, respectively, were each rotated in 15° increments through 360°, giving a 24 × 24 matrix or 576 optimized structures (Scheme 4). Torsion angles C1′−C2′−O2′−H (θ_1), C3−C2−O2−H (θ_2), and C4−C3−O3−H (θ_3) were fixed at 180°. The remaining seven exocyclic torsion angles in **2** were held constant or were set at an initial value and optimized, as summarized in Scheme 4. Six additional datasets were generated for **2**, in which θ_1, θ_2, or θ_3 was fixed at either 60 or 300°, while the other ring C−O torsion angles were fixed at 180°, each set containing 576 structures.

Scheme 4. Torsion Angle Constraints Used in DFT Calculations of Nonconventional Spin-Coupling Constants in 2[a]

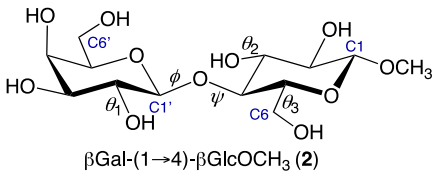

βGal-(1→4)-βGlcOCH$_3$ (**2**)

C2–C1–O1–CH$_3$: Initial, 180°
C3–C2–O2–H: Fixed, 180°
C4–C3–O3–H: Fixed, 60°, 180°, 300° (θ_2)
C4–C5–C6–O6: Fixed, 60°, 180°, 300° (θ_3)
C5–C6–O6–H: Fixed, 180°
C1′–C2′–O2′–H: Fixed, 60°, 180°, 300° (θ_1)
C2′–C3′–O3′–H: Fixed, 180°
C3′–C4′–O4′–H: Fixed, 180°
C4′–C5′–C6′–O6′: Fixed, 180°
C5′–C6′–O6′–H: Fixed, 180°

phi (ϕ): O5′–C1′–O1′–C4: 15° rotations
psi (ψ): C1′–O1′–C4–C3: 15° rotations

[a]Exocyclic torsion angles θ_1, θ_2, and θ_3 were sampled in three perfectly staggered geometries, yielding 27 datasets containing incremental rotations of φ and ψ through 360°. See text for details.

For structures **3**−**7**, the ϕ and ψ torsion angles were each rotated in 15° increments through 360°, giving 24 × 24 matrices (576 structures). Only one set of exocyclic torsion angles was investigated in **3**−**7** as summarized in Schemes S4−S8 (Supporting Information). In DFT calculations of **5** and **7**, deoxy analogs were used to simplify the structures and/or avoid unfavorable steric interactions when the ϕ and ψ torsion angles were rotated. The deoxy sites were kept to a minimum and judged based on prior work to be sufficiently distant from the coupling pathways of interest to not influence their calculated behaviors.

2.2. Calculations of NMR Spin-Coupling Constants. A group *of* J_{HH}, J_{CH}, and J_{CC} *s*pin-coupling constants with potentially useful dependencies on ϕ or ψ was calculated in geometry optimized structures of **2**−**7** by DFT using the B3LYP functional[17,18] in *Gaussian*09.[16] The Fermi contact,[22−24] diamagnetic and paramagnetic spin−orbit, and spin-dipole terms[22] were recovered using a tailored basis set, [5s2p1d|3s1p],[25,26] and raw (unscaled) calculated spin-couplings are reported and are similar to experimental values to within ±0.2−0.3 Hz based on prior work.[26,27] SCRF[20] and the IEFPCM[21] were again used to treat the effects of solvent water during *J*-coupling calculations.

DFT calculations of $^1J_{CH}$, $^1J_{CC}$, $^3J_{CH}$, and $^3J_{CC}$ values gave positive signs as expected, whereas those of $^2J_{CH}$ and $^2J_{CC}$ values gave either positive or negative signs. Experimental sign determinations of the latter geminal *J*-couplings have been reported in prior work,[28−32] and ample comparisons have been made between experimental and calculated signs to validate those obtained by DFT calculations.

2.3. Spin-Coupling Constant Equation Parameterization. Equations relating DFT-calculated J_{HH}, J_{CH}, and J_{CC} values to ϕ or ψ in **2**−**7** were parameterized to a trigonometric polynomial using R. Equations were parameterized using *J*-values calculated in a subpopulation of conformers that was selected using a 10 kcal/mol energy cut-off to remove a limited number of highly structurally strained conformers.[10,12] A secondary constraint was also applied when necessary to remove DFT-optimized structures containing distorted aldohexopyranosyl rings; Cremer-Pople puckering parameters were calculated from DFT-generated Cartesian coordinates, and a θ value of 35° was used as the cut-off.[10,12] The goodness-of-fit of each equation is reported as a root mean squared deviation (RMSD). Equation parameterization was further evaluated using the Akaike information criterion,[33] resulting in truncated forms of two equations.

3. RESULTS AND DISCUSSION

3.1. Potential Nonconventional Spin-Coupling Constraints for ϕ. Criteria to determine whether a specific *J*-coupling may have value in *MA'AT* analyses of ϕ and ψ include: (1) dynamic range; (2) character of the torsion angle versus *J*-value plot (e.g., does the plot contain multiple maxima and minima?); (3) whether the *J*-value exhibits a significant secondary dependence on either ϕ or ψ; (4) whether the *J*-value exhibits other significant structural dependencies in addition to either ϕ or ψ (e.g., dependencies on proximal exocyclic C−O torsion angles); and (5) whether the experimental *J*-value can be conveniently and accurately measured and its sign determined if required, preferably without the need for stable isotopic labeling. Secondary dependencies or effects (criterion 3) refer to *J*-coupling behaviors where *J*-coupling depends primarily on one torsion angle but also shows dependencies on a second or third torsion angle. In the present work, a *J*-coupling might depend heavily on ϕ but also show some dependence on ψ or vice versa. Secondary dependencies can complicate the structural interpretations of *J*-couplings if they are not well understood and accounted for. In the following discussion, potential nonconventional *J*-couplings are identified that satisfy most, if not all, of these criteria.

Five nonconventional *J*-couplings to evaluate ϕ are shown in Scheme 5, illustrated in **2** although analogous *J*-couplings exist in disaccharides **3**−**7** (Scheme 3). These couplings include $^1J_{C1',H1'}$, $^1J_{C1',C2'}$, $^2J_{C1',H2'}$, $^2J_{C2',H1'}$, and $^4J_{H1',H4}$. $^1J_{C1',H1'}$ and $^1J_{C1',C2'}$ are expected to depend on ϕ, based on anticipated

https://doi.org/10.1021/acsomega.2c02793
ACS Omega 2022, 7, 23950−23966

Scheme 5. Nonconventional Spin-Coupling Constants That May Depend on φ, Illustrated for the Internal *O*-Glycosidic Linkage in 2[a]

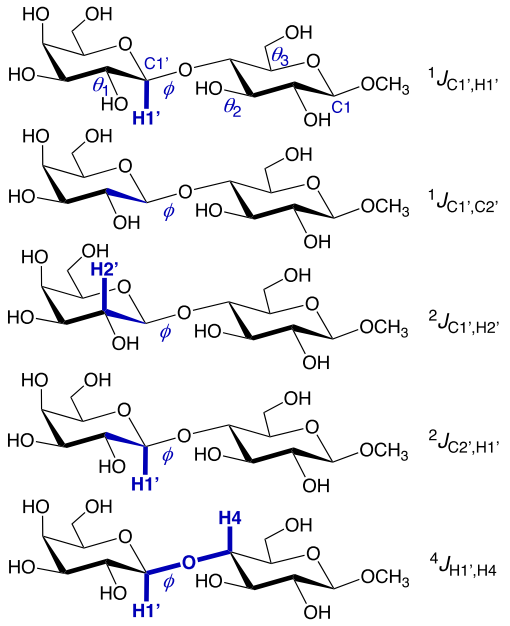

[a]Coupling pathways are highlighted in blue. Torsion angles θ_1, θ_2, and θ_3 denote rotations about the C2′−O2′, C3−O3, and C5−C6 bonds, respectively.

vicinal lone-pair effects on C−H and C−C bond lengths caused by rotation of the C1′−O1′ bond (ϕ). The C1′−H1′ and C1′−C2′ bond lengths are affected by $n\rightarrow\sigma^*$ donation when a lone-pair orbital on O1′ is anti to the bond, in general leading to bond elongation[34,35] (in the ensuing discussion, oxygen atoms are assumed to bear two sp^3-hybridized lone-pair orbitals although other lone-pair arrangements may pertain[36−38]). Presumably the percent *s*-character of both bonds is greater (shorter bonds) for geometries in which both O1′ lone-pairs are gauche to them. For $^1J_{C1',C2'}$, overlapping vicinal lone-pair effects from C2′−O2′ bond rotation (θ_1) also pertain. Thus, at least two structural factors influence $^1J_{C1',C2'}$, namely, rotation about ϕ and θ_1. Superimposed on these stereoelectronic effects may be bond angle effects caused by the rotation of ϕ and θ_1.

Geminal $^2J_{C1',H2'}$ and $^2J_{C2',H1'}$ values are expected to have strong configurational dependencies superimposed on conformational dependencies on ϕ and θ_1. Consider the generalized $C_a-C_b-H_b$ coupling pathway shown in Scheme 6. Rotation of the C_a-C_b bond (γ_1) describes the configurational dependence of $^2J_{Ca,Hb}$, manifested in both coupling magnitude and sign. For $^2J_{C1',H2'}$ and $^2J_{C2',H1'}$ in **2**, rotation about the analogous C1′−C2′ bond is constrained by the pyranosyl ring (i.e., the configuration is fixed) such that this constraint determines their baseline magnitudes and signs. C−O Bond rotations γ_2 and γ_3 are mainly responsible for the conformational dependencies of $^2J_{Ca,Hb}$. In general, for the $C_a-C_b-H_b$ pathway, the effect of rotation of γ_3 is greater than that for rotation of γ_2; that is, rotation of the C−O bond involving the carbon bearing the coupled hydrogen exerts a greater effect on $^2J_{Ca,Hb}$ than rotation of the C−O bond involving the coupled carbon. The difference in sensitivity is ∼2−3 fold.[39,40] Thus, while $^2J_{C1',H2'}$ might be a potential constraint on ϕ (Scheme 5), rotation of ϕ exerts a smaller effect on the coupling than rotation of θ_1, reducing the dynamic range and consequently its usefulness as a ϕ constraint. Conversely, rotation of ϕ exerts a greater effect on $^2J_{C2',H1'}$ than rotation of θ_1. Thus, all else being equal, $^2J_{C2',H1'}$ is likely to be the better probe of ϕ than $^2J_{C1',H2'}$. However, even in this case, contributions from θ_1 to $^2J_{C2',H1'}$ cannot be ignored (i.e., independent information on θ_1 would be desirable to determine its contribution to the magnitude of experimental $^2J_{C2',H1'}$ values in solution).

Scheme 6. Bond Torsions γ_1, γ_2, and γ_3 That Influence the Magnitude and Sign of $^2J_{Ca,Hb}$ (Pathway Highlighted in Blue)[a]

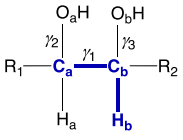

[a]R_1 and R_2 are assumed to be sp^3-hybridized carbons as found in typical saccharide carbon scaffolds.

$^4J_{H1',H4}$ is likely to exhibit sensitivities to both ϕ and ψ.[40−42] If this behavior is confirmed by DFT calculations, $^4J_{H1',H4}$ values may serve only as independent tests of the conformational models of ϕ and ψ determined from more robust *J*-values (see discussion below). Even in this role, the very small dynamic range of $^4J_{H1',H4}$ will limit its use in assignments of linkage conformation.

3.2. Potential Nonconventional Spin-Coupling Constraints for ψ.

In **2**, nine nonconventional *J*-couplings have the potential to serve as constraints on ψ (Scheme 7): $^1J_{C4,H4}$, $^1J_{C3,C4}$, $^1J_{C4,C5}$, $^2J_{C3,H4}$, $^2J_{C4,H3}$, $^2J_{C5,H4}$, $^2J_{C4,H5}$, $^2J_{C3,C5}$, and $^4J_{H1',H4}$. Analogous *J*-values exist in disaccharides **3**−**7**. The structural dependencies of the $^1J_{CH}$, $^1J_{CC}$, and $^2J_{CCH}$ values are expected to mimic those sensitive to ϕ (Scheme 5). For example, $^1J_{C3,C4}$ will depend on the rotameric properties of the C3−C4, C3−O3 (θ_2), and C4−O1′ (ψ) bonds.[43] Since rotation about the C3−C4 bond is constrained by the pyranosyl ring, only the remaining C−O bonds will largely determine $^1J_{C3,C4}$ in solution. Likewise, $^2J_{C3,H4}$ and $^2J_{C5,H4}$ are likely to be better constraints on ψ than $^2J_{C4,H3}$ and $^2J_{C4,H5}$ (see above discussion of Scheme 6). $^4J_{H1',H4}$ is likely to serve as an independent test of the conformational models of ψ (and ϕ) determined from more robust *J*-values.

The geminal $^{13}C-^{13}C$ spin-coupling, $^2J_{C3,C5}$, is expected to show configurational and conformational dependencies analogous to those of $^2J_{C1,C3}$ in aldopyranosyl rings.[40,44] Configuration at the terminal coupled carbons affects its magnitude and sign, especially O3 orientation (axial vs equatorial), while the effect of configuration at the intervening C4 carbon is expected to be small. Conformational effects derive from rotation of the C3−O3 (θ_2), C5−C6 (θ_3), and C4−O1′ (ψ) bonds, with ψ exerting a greater effect than θ_2 and θ_3. In **2**, the configurational effects are fixed and determine the baseline value of $^2J_{C3,C5}$ in solution. This value will vary in response to the conformational effects. Consequently, the reliability of $^2J_{C3,C5}$ as a probe of ψ in solution will depend on the degree to which the contributions from θ_2 and θ_3 can be determined.

3.3. DFT Calculations of Nonconventional ϕ-Dependent Spin-Coupling Constants in 2.

$^1J_{C1',H1'}$, $^2J_{C1',H2'}$, $^2J_{C2',H1'}$, and $^1J_{C1',C2'}$ were calculated as a function of ϕ in **2**

https://doi.org/10.1021/acsomega.2c02793
ACS Omega 2022, 7, 23950−23966

Scheme 7. Potential Nonconventional Spin-Coupling Constants That May Depend on ψ, Illustrated for the Internal *O*-Glycosidic Linkage in 2[a]

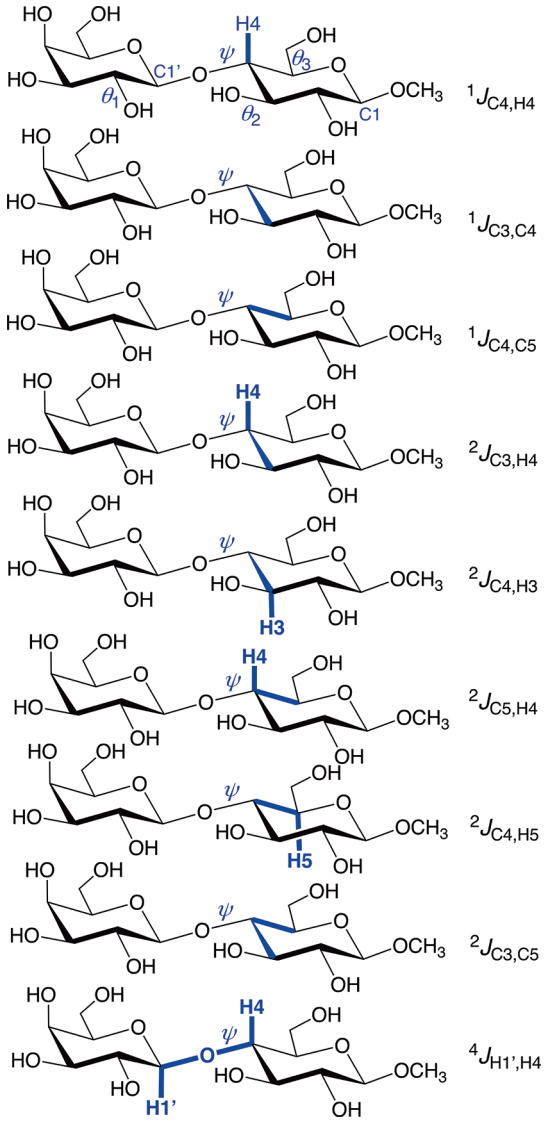

[a]Coupling pathways are highlighted in blue. Torsion angles θ_1, θ_2, and θ_3 denote rotations about the C2′−O2′, C3−O3, and C5−C6 bonds, respectively.

(Figure 1). Scatter along the *y*-axis at discrete values of ϕ shows the secondary effect of ψ. The plots for $^1J_{C1',H1'}$ and $^2J_{C1',H2'}$ contain significant scatter, indicating that neither *J*-value will be a reliable independent constraint for ϕ. The dynamic range for $^2J_{C1',H2'}$ is also small (~1 Hz), further reducing its usefulness. The shape of the curve can be understood by noting the calculated $^2J_{C1',H2'}$ values in the three idealized staggered rotamers of ϕ (rotamers I−III, Scheme 8) and inspecting the corresponding Newman projections. Less negative values correlate with ϕ rotamers in which a lone-pair orbital on O1′ is *anti* to the C1′−C2′ bond (rotamers II and III). In contrast to $^2J_{C1',H2'}$, $^2J_{C2',H1'}$ displays a larger dynamic range (4−5 Hz) when its sign is taken into account, rendering it a better probe of ϕ than $^2J_{C1',H2'}$ (Figure 1C). The $^2J_{C2',H1'}$ plot also has considerably less *y*-axis scatter, especially at ϕ values of 0−180° (i.e., $^2J_{C2',H1'}$ has less *y*-axis scatter overall than observed for $^2J_{C1',H2'}$). In the three idealized staggered ϕ rotamers shown in Scheme 8, the calculated $^2J_{C2',H1'}$ is more positive in III (~3 Hz) than in I and II (~0−1 Hz). In III, the C1′−H1′ and C1′−C2′ bonds are both *anti* to an O1′ lone-pair orbital, whereas in I and II, a lone-pair orbital is *anti* to only one of these bonds. These lone-pair orbital effects on $^2J_{CCH}$ are consistent with those reported previously.[39,40]

Like $^2J_{C2',H1'}$, the plot for $^1J_{C1',C2'}$ shows modest *y*-axis scatter and a relatively large dynamic range (~6 Hz). Rotamers II and III (Scheme 8) contain an O1′ lone-pair orbital *anti* to the C1′−C2′ bond, and both give $^1J_{C1',C2'}$ values of ~49 Hz. In contrast, both O1′ lone-pair orbitals are *gauche* to the C1′−C2′ bond in **1**, yielding a $^1J_{C1',C2'}$ of ~53 Hz. These observations are consistent qualitatively with the discussion above, namely, that rotamers II and III are likely to contain longer C1′−C2′ bonds than rotamer I, resulting in less *s*-character and a smaller $^1J_{C1',C2'}$.

3.4. DFT Calculations of Nonconventional ψ-Dependent Spin-Coupling Constants in 2. The dependencies of $^1J_{C4,H4}$, $^1J_{C3,C4}$, and $^1J_{C4,C5}$ on ψ in **2** are shown in Figure 2. $^1J_{C4,H4}$ behaves similarly to $^1J_{C1',H1'}$ (Figure 1A) with regard to *y*-axis scatter, indicating that, like $^1J_{C1',H1'}$, $^1J_{C4,H4}$ is unlikely to be a useful constraint for ψ. $^1J_{C3,C4}$ and $^1J_{C4,C5}$ are more promising, with both showing moderate secondary dependencies on ϕ and adequate dynamic ranges (6−7 Hz). Newman projections of the O1′−C4 bond in **2** for the three idealized staggered rotamers IV−VI of ψ (Scheme 9) provide structural rationales for the behaviors of $^1J_{C3,C4}$ and $^1J_{C4,C5}$. $^1J_{C3,C4}$ in rotamers V and VI (~43 Hz) is smaller than that in rotamer IV (~47 Hz), while $^1J_{C4,C5}$ is smaller in rotamers IV and V (~41 Hz) than in rotamer VI (~46 Hz). Rotamers V and VI contain an O1′ lone-pair orbital *anti* to the C3−C4 bond, but rotamer IV does not, leading to a smaller $r_{C3,C4}$ in IV relative to V and VI and presumably to the larger $^1J_{C3,C4}$ in IV. Similarly, rotamers IV and V contain an O1′ lone-pair orbital *anti* to the C4−C5 bond, whereas rotamer VI does not, resulting in a plot of $^1J_{C4,C5}$ that mimics that observed for $^1J_{C3,C4}$ (plots B and C in Figure 2 are essentially phase-shifted along the *x*-axis).

The dependences of the four $^2J_{CCH}$ values in Scheme 7 on ψ in **2** are shown in Figure 3. The dynamic ranges for $^2J_{C4,H3}$ (~1.5 Hz) and $^2J_{C4,H5}$ (~1.5 Hz) are small, and neither *J*-coupling is likely to be a useful constraint for ψ. In contrast, the dynamic ranges of $^2J_{C3,H4}$ (~2 Hz) and $^2J_{C5,H4}$ (~5 Hz) are larger, especially the latter. The plot of $^2J_{C5,H4}$ indicates more negative values in rotamers V and VI relative to rotamer IV. In rotamer IV, O1′ lone-pair orbitals are *anti* to both the C4−H4 and C4−C5 bonds, whereas in rotamers V and VI, a lone-pair orbital is *anti* to only one of these bonds. This situation mimics that observed for $^2J_{C2',H1'}$ where the less negative (more positive) *J*-coupling is associated with rotamer III (Figure 1C, Scheme 8). Applying the same analysis to $^2J_{C3,H4}$ (Figure 3A) leads to the prediction that rotamer VI should give a less negative (more positive) *J*-coupling than rotamers IV and V since it contains O1′ lone-pairs *anti* to both the C3−C4 and C4−H4 bonds (Scheme 9). The plot in Figure 3A supports this prediction, although rotamers IV and V yield different, albeit more negative values. Orienting an O1′ lone-pair *anti* to the C3−C4 bond (rotamer V) appears to reduce $^2J_{C3,H4}$ more significantly than orienting a lone-pair *anti* to the C4−H4 bond (rotamer IV).

Rotamer IV is associated with a more negative $^2J_{C4,H5}$ than rotamer V even though both contain an O1′ lone-pair orbital anti to the C4−C5 bond, but the most negative value, as

https://doi.org/10.1021/acsomega.2c02793
ACS Omega 2022, 7, 23950−23966

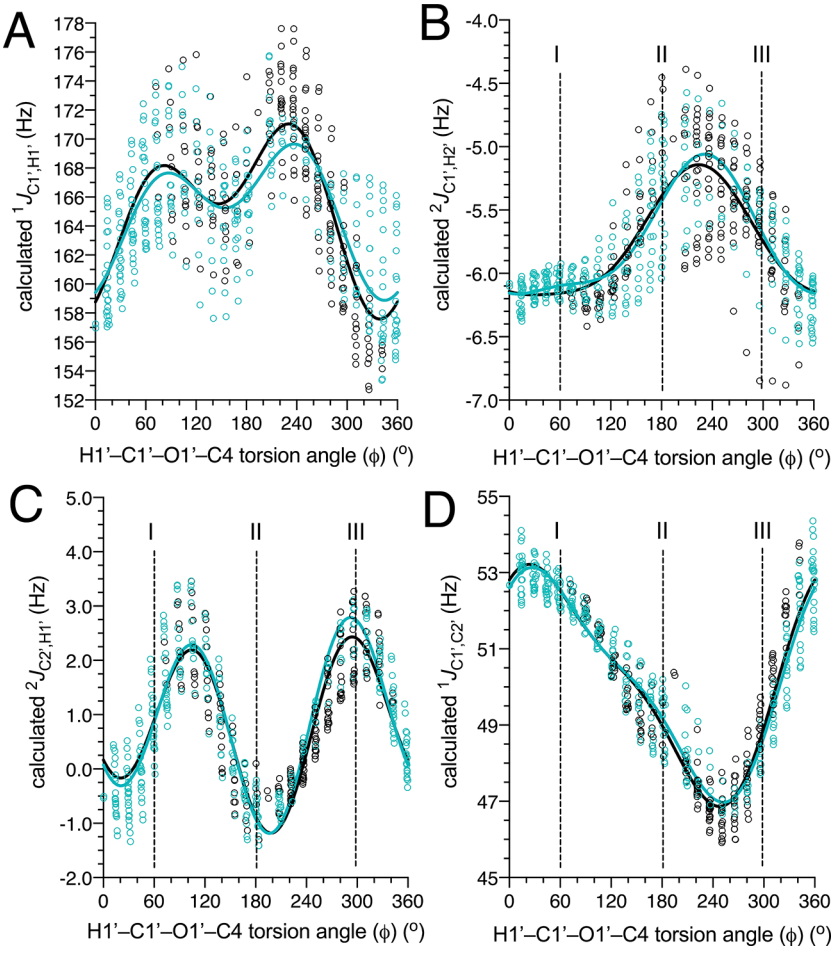

Figure 1. Calculated dependencies of $^{1}J_{C1',H1'}$ (A), $^{2}J_{C1',H2'}$ (B), $^{2}J_{C2',H1'}$ (C) and $^{1}J_{C1',C2'}$ (D) on ϕ in **2**. Black circles, full dataset; green circles, trimmed dataset. Solid green and black lines represent best fits to the green and black datasets, respectively. See Scheme 8 for the definitions of ϕ rotamers I–III identified in each plot. The scatter observed at discrete ϕ values in these plots reveals the secondary dependencies on ψ.

Scheme 8. Idealized Staggered Rotamers I–III of the C1′–O1′ Bond φ in 2[a]

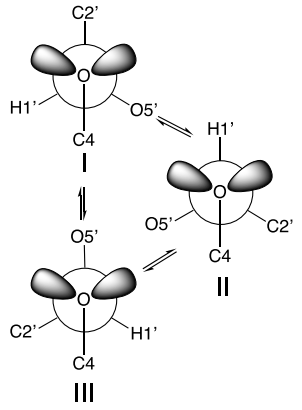

[a]The *exo*-anomeric effect favors rotamer I in the β-linkage of **2**. One lone-pair orbital on O1′ is *anti* to the C1′–C2′ bond in II and III, whereas both orbitals are *gauche* to this bond in I.

expected, is associated with rotamer VI which lacks this interaction (Scheme 9). Likewise, rotamers V and VI are expected to be associated with more positive $^{2}J_{C4,H3}$ values than rotamer IV since the former contain an O1′ lone-pair orbital anti to the C3–C4 bond and the latter does not. In addition to vicinal lone-pair effects, longer-range 1,3 lone-pair effects[40] from O1′ on the C3–H3 or C5–H5 bond lengths may influence the behaviors of $^{2}J_{C4,H3}$ and $^{2}J_{C4,H5}$, but these effects cannot be visualized using the projections in Scheme 9.

Collectively, the nonconventional $^{2}J_{CCH}$ values in **2** behave similarly with respect to the effects of oxygen vicinal lone-pair orbitals on coupling magnitude and sign. The presence of an oxygen lone-pair *anti* to either the C–C or C–H bond of the coupling pathway, or to both bonds, shifts the coupling to a more positive (less negative) value relative to the coupling observed in conformations lacking these *anti* arrangements. The lone-pair effects appear additive, although they are probably not equivalent, that is, the effect of a lone-pair *anti* to the C–C bond may be larger than when *anti* to the C–H bond. These conclusions are consistent with those drawn in an earlier study of the conformational dependencies of $^{2}J_{CCH}$ values in saccharides.[39,40]

$^{2}J_{C3,C5}$ shows a bimodal dependence on ψ and is positive in sign with a dynamic range of ~3 Hz (Figure 4). Rotamers IV and VI correlate with smaller values (~2 Hz) than rotamer V (~4 Hz). In rotamer V, the two lone-pair orbitals on O1′ are *anti* to the C3–C4 and C4–C5 bonds (the two bonds comprising the coupling pathway), whereas in rotamers IV and VI only one of these lone-pair interactions exists (the remaining lone-pair orbital is *anti* to the C4–H4 bond). Prior studies have shown that the lone-pair arrangements in

https://doi.org/10.1021/acsomega.2c02793
ACS Omega 2022, 7, 23950–23966

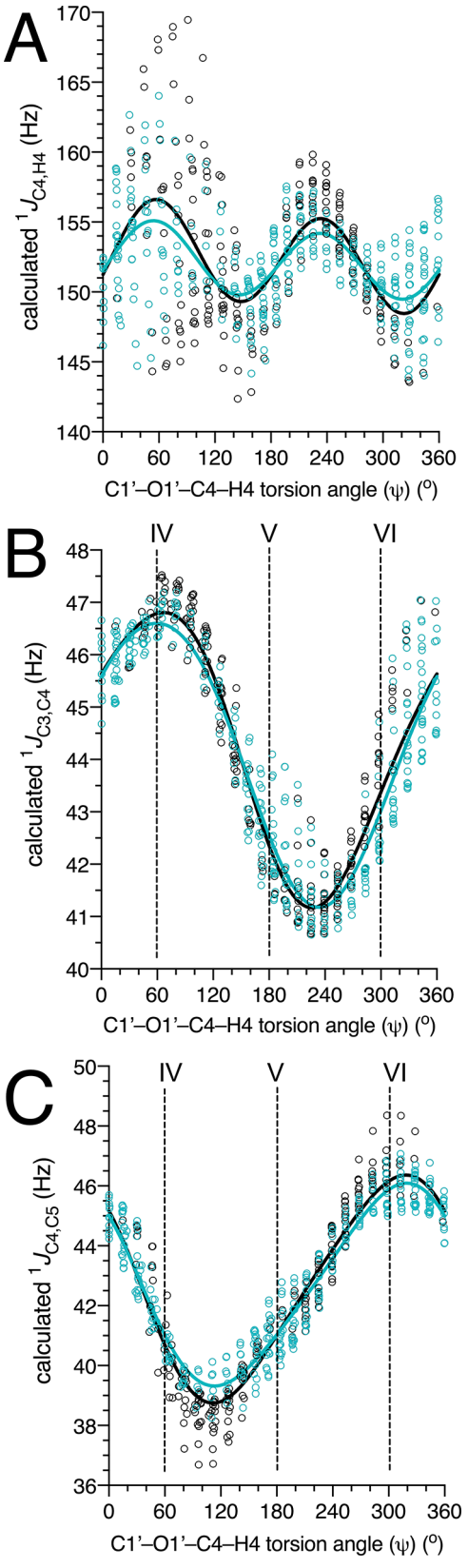

Figure 2. Calculated dependencies of $^1J_{C4,H4}$ (A), $^1J_{C3,C4}$ (B), and $^1J_{C4,C5}$ (C) on ψ in **2**. See Figure 1 for the definitions of the green and black data points and lines. Scheme 9 contains the definitions of ψ rotamers IV–VI. The scatter observed at discrete ψ values in these plots reveals the secondary dependencies on ϕ.

Scheme 9. Idealized Staggered Rotamers IV–VI of the C4–O1′ Bond ψ in 2

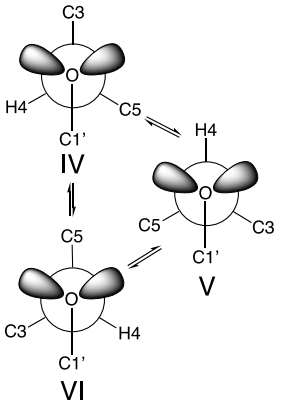

rotamer V shift $^2J_{CCC}$ to more positive values in saccharides (i.e., this relationship pertains to $^2J_{C1,C3}$, $^2J_{C2,C4}$, and $^2J_{C4,C6}$ in aldohexopyranosyl rings).[39,40]

Based on evaluations in Sections 3.3 and 3.4 above, the following seven nonconventional spin-coupling constants in Schemes 5 and 7 are good candidates for *MA'AT* modeling of ϕ and ψ in **2**: for ϕ, $^1J_{C1',C2'}$ and $^2J_{C2',H1'}$; for ψ, $^1J_{C3,C4}$, $^1J_{C4,C5}$, $^2J_{C3,H4}$ (marginal), $^2J_{C5,H4}$, and $^2J_{C3,C5}$. By extension, related *J*-couplings in other two-bond *O*-glycosidic linkages (e.g., those in **3**–**7**, Scheme 3) should prove useful for *MA'AT* modeling of their linkages, as discussed below.

3.5. Effects of Exocyclic C–O Bond Conformation on ϕ- and ψ-Dependent Nonconventional Spin-Couplings Constants in 2. Having identified seven potentially useful nonconventional ϕ- and ψ-dependent *J*-couplings, secondary conformational effects that influence them were evaluated. In the treatments discussed above, the effects of ϕ or ψ on these *J*-couplings were studied. All other exocyclic conformational features were fixed or highly constrained in geometries dictated by the ten torsion angles shown in Scheme 4. Superimposed on these ϕ and ψ dependencies are secondary conformational dependences whose magnitudes need to be understood and quantified in order to apply these nonconventional *J*-couplings to structural studies. These secondary dependencies arise largely from exocyclic C–O bond torsion angles θ_1–θ_3 (Scheme 5), and Scheme 10 shows which of these angles affect specific ϕ- and ψ-dependent non-conventional *J*-couplings. For example, for $^1J_{C1',C2'}$ and $^2J_{C2',H1'}$, rotation about θ_1 affects their magnitudes and/or signs, in addition to rotation about ϕ. In a similar vein, $^1J_{C3,C4}$ and $^2J_{C3,H4}$ are affected by θ_2 in addition to ψ. In the following discussion, the secondary effects of θ_1, θ_2, and θ_3 are discussed in more detail.

3.5.1. $^1J_{C1',C2'}$ and $^2J_{C2',H1'}$ (ϕ-Dependent). Plots of $^1J_{C1',C2'}$ as a function of ϕ adopt the same overall shape regardless of the values of θ_1, θ_2, and θ_3 (Figure 5A). However, a *y*-axis displacement of ~5 Hz to smaller $^1J_{C1',C2'}$ is observed for θ_1 rotamers VII and IX relative to the remaining curves, including that for θ_1 rotamer VIII (reference state) (Scheme S1, Supporting Information). An inspection of θ_1 rotamers shows that an O2′ lone-pair orbital is *anti* to C1′ in rotamers VII and IX but not in VIII. The former geometry is expected to lengthen the C1′–C2′ bond (vicinal lone-pair interaction), leading to smaller $^1J_{C1',C2'}$ values.

The effects of θ_1–θ_3 on $^2J_{C2',H1'}$ are modest (~0.5 Hz) except for the curve for rotamer XV (Scheme S3, Supporting

https://doi.org/10.1021/acsomega.2c02793
ACS Omega 2022, 7, 23950–23966

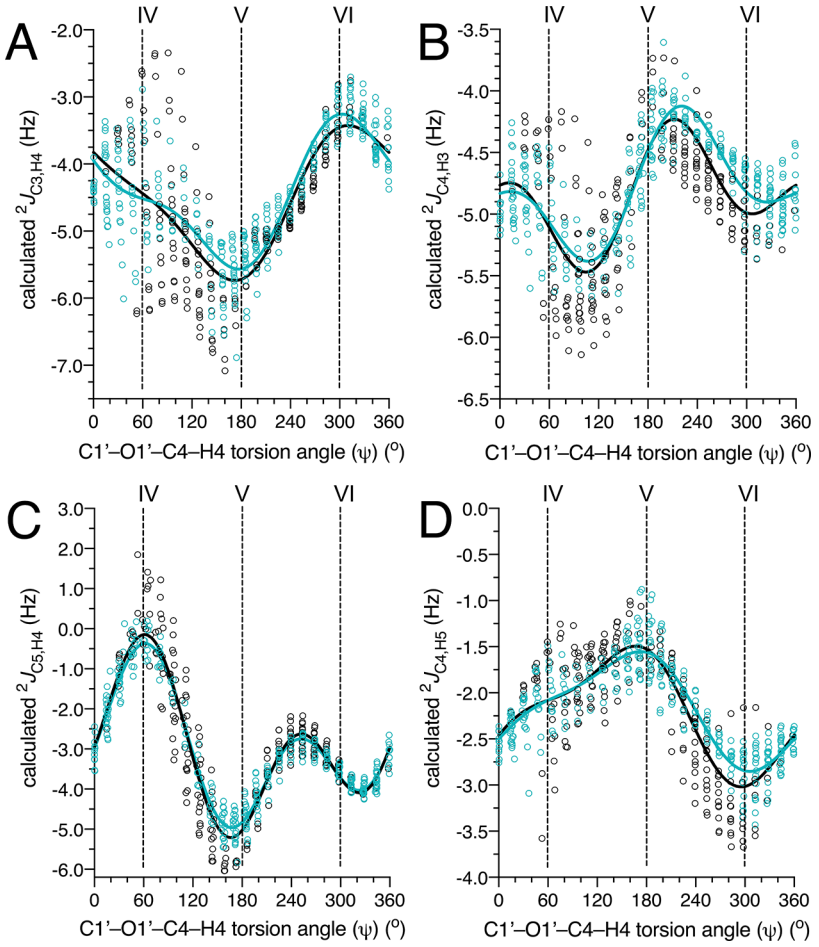

Figure 3. Calculated dependencies of $^2J_{C3,H4}$ (A), $^2J_{C4,H3}$ (B), $^2J_{C5,H4}$ (C), and $^2J_{C4,H5}$ (D) on ψ in **2**. See Figure 1 for definitions of the green and black data points and lines, and Scheme 9 for the definitions of ψ rotamers IV–VI. The scatter observed at discrete ψ values in these plots reveals the secondary dependencies on ϕ.

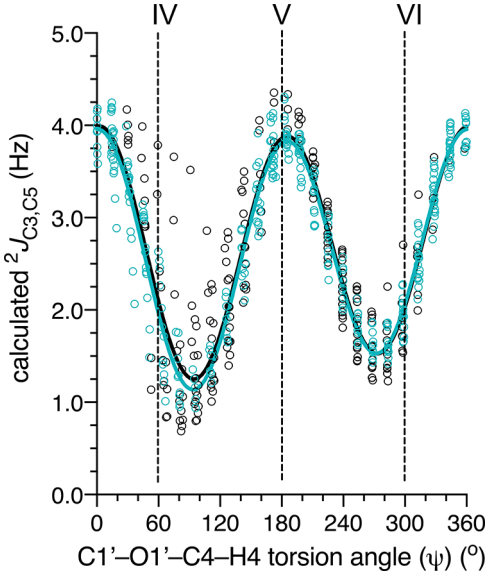

Figure 4. Calculated dependency of $^2J_{C3,C5}$ on ψ in **2**. See Figure 1 for the definitions of the green and black data points and lines, and Scheme 9 for the definitions of ψ rotamers IV–VI. The scatter observed at discrete ψ values reveals the secondary dependence on ϕ.

Scheme 10. Secondary Effects of Torsion Angles θ_1, θ_2, and θ_3 on Seven Nonconventional Spin-Coupling Constants Sensitive to φ and ψ in 2[a]

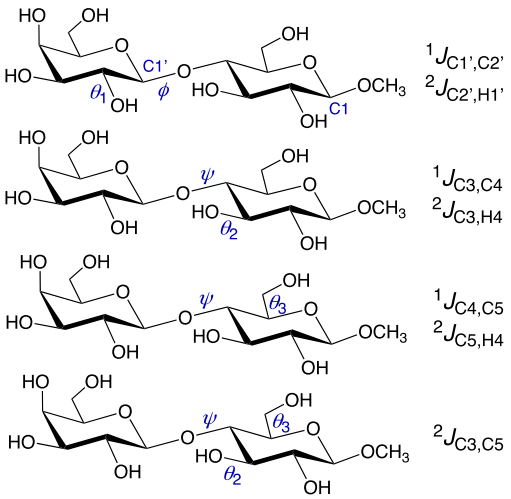

[a]For each set of *J*-couplings shown on the right, the torsion angle(s) shown in blue affect their magnitudes and/or signs.

Information) near ϕ values of 300° (Figure 5B). $^2J_{C2',H1'}$ values are most positive when the two lone-pair orbitals on O2′ are *anti* to the C1′–C2′ and C2′–C3′ bonds (θ_1 rotamer IX). The

https://doi.org/10.1021/acsomega.2c02793
ACS Omega 2022, 7, 23950–23966

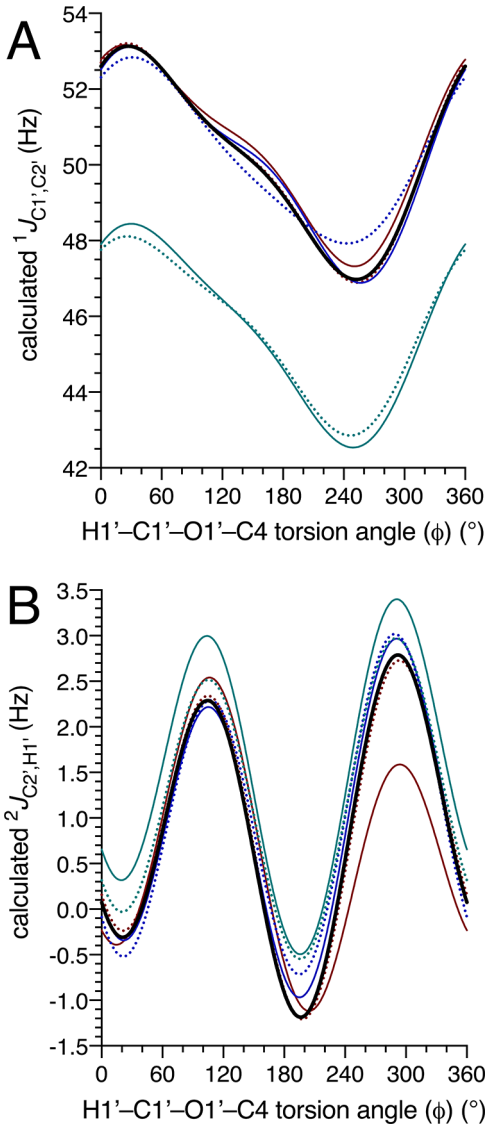

Figure 5. Effects of θ_1−θ_3 on the dependencies of $^1J_{C1',C2'}$ (A) and $^2J_{C2',H1'}$ (B) on ϕ in **2**. For each plot: black line, reference state; green dots, rotamer VII; green line, rotamer IX; blue dots, rotamer X; blue line, rotamer XII; red dots, rotamer XIII; red line, rotamer XV. For the definitions of rotamers and reference states, see Schemes S1−S3, Supporting Information.

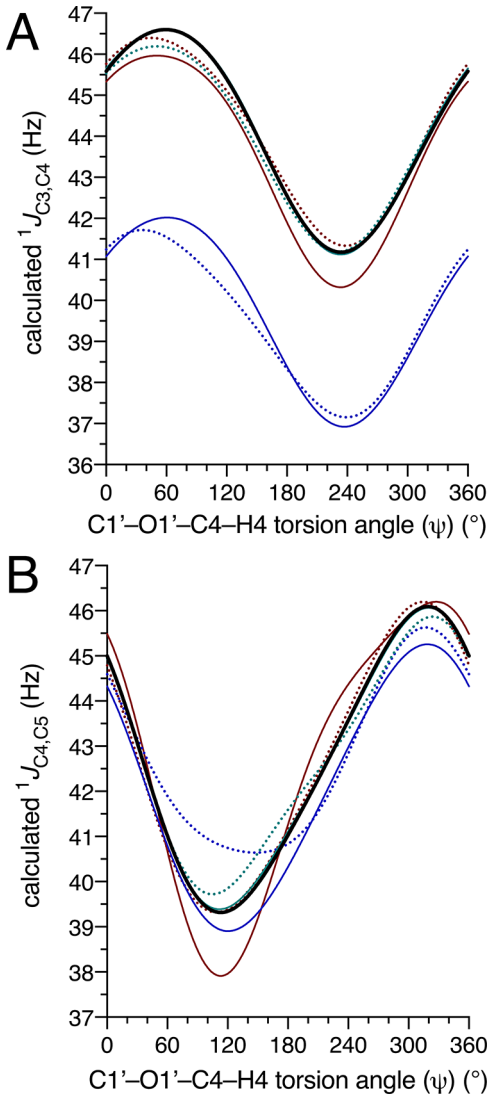

Figure 6. Effects of θ_1−θ_3 on the dependencies of $^1J_{C3,C4}$ (A) and $^1J_{C4,C5}$ (B) on ψ in **2**. For each plot: black line, reference state; green dots, rotamer VII; green line, rotamer IX; blue dots, rotamer X; blue line, rotamer XII; red dots, rotamer XIII; red line, rotamer XV. For the definitions of rotamers and reference states, see Schemes S1−S3, Supporting Information.

behavior in rotamer XV at ϕ near 300° probably results from greater data scatter from the secondary ψ dependence and its effect on parameterization since in these ϕ geometries, O2′ and O6 are in close proximity in some ψ rotamers. These findings show that rotation of the C−O bond involving the coupled carbon (in this case, θ_1) exerts a smaller effect on $^2J_{CCH}$ than rotation of the C−O bond involving the carbon bearing the coupled hydrogen (in this case, ϕ) (Scheme 6).

3.5.2. $^1J_{C3,C4}$ and $^1J_{C4,C5}$ (ψ-Dependent). The dependence of $^1J_{C3,C4}$ on ψ (Figure 6A) mimics that of $^1J_{C1',C2'}$ on ϕ (Figure 5A) in that both curves are unimodal, although the former *J*-couplings are smaller by 6−7 Hz (the C3−C4 fragment bears only two oxygen substituents, whereas the C1′−C2′ fragment bears three). $^1J_{CC}$ decreases in magnitude as the number of oxygen substituents on the C−C fragment declines. Secondary effects may pertain when two oxygen substituents are involved in terms of whether both reside on the same carbon or different carbons. The effects of θ_1−θ_3 on curve shape are small, but the curves associated with θ_2 rotamers X and XII are shifted to smaller values by ∼5 Hz relative to θ_2 rotamer XI (reference state). An inspection of Scheme S2 (Supporting Information) shows an O3 vicinal lone-pair interaction with the C3−C4 bond in rotamers X and XII but not in rotamer XI. As found for $^1J_{C1',C2'}$, lengthening of the C3−C4 bond in the former two rotamers leads to smaller $^1J_{CC}$ values.

The curves for $^1J_{C4,C5}$ are unimodal (Figure 6B) and are affected to a limited extent by θ_1−θ_3. The effect of θ_1 is small but not that of θ_2, especially for rotamer X. Exocyclic hydroxymethyl group conformation affects $^1J_{C4,C5}$, with the curve for rotamer XV (*tg*) differing from those for rotamers XIII (*gg*) and XIV (*gt*). The hydroxymethyl group effects are probably caused by significant data scatter at ψ values of 60−180° where strong steric interactions between O5′ and the C6−O6 fragment occur, especially in the *tg* rotamer. This scatter may influence curve parameterization and render

https://doi.org/10.1021/acsomega.2c02793
ACS Omega 2022, 7, 23950−23966

comparisons unreliable. For ψ values devoid of steric interactions (values of 0−60° and 180−360°), the curves are very similar (y-axis displacements of ≤1 Hz).

3.5.3. $^2J_{C3,H4}$, $^2J_{C5,H4}$, and $^2J_{C3,C5}$ (ψ-Dependent). The effects of θ_1−θ_3 on the dependence of $^2J_{C3,H4}$ on ψ are modest (differences of ∼0.5 Hz) (Figure 7A). The single outlier is θ_3 rotamer XV (*tg*; Scheme S3, Supporting Information), and aberrant parameterization caused by significant data scatter at ψ values of 150−200° (steric clashes) is probably the cause. The effect of θ_1 is negligible (remote rotation), but a small θ_2 effect (rotation of the C3−O3 bond) is observed. $^2J_{C3,H4}$ values associated with rotamers X and XII are more positive (less negative) by ∼0.5 Hz than those associated with rotamer XI (reference state). C3−O3 Rotamers containing O3 lone-pair orbitals *anti* to the C2−C3 and C3−C4 bonds (θ_2 rotamer XII) or one O3 lone-pair orbital *anti* to the C3−C4 bond (θ_2 rotamer X) yield slightly more positive (less negative) $^2J_{C3,H4}$ values than rotamer XI that lacks either of these arrangements. Similar behavior was observed for $^2J_{C2',H1}$ (Figure 5B).

The effects of θ_1−θ_3 on the dependencies of $^2J_{C5,H4}$ and $^2J_{C3,C5}$ on ψ (Figure 7B,C) are small (<1 Hz); curve shapes are highly conserved. Rotation of θ_3 does not affect $^2J_{C5,H4}$ despite the proximity of the exocyclic hydroxymethyl group to the C5−C4−H4 coupling pathway. Rotation of θ_2 also does not much affect $^2J_{C5,H4}$ despite potential 1,3-lone-pair interactions between O3 lone-pair orbitals and the proximal C4−H4 bond.

Rotations of θ_2 and θ_3 exert small effects on $^2J_{C3,C5}$. The available data indicate that θ_2 rotamers that orient one of the O3 lone-pair orbitals anti to the C3−C4 bond (rotamers X and XII; Scheme S2, Supporting Information) shift $^2J_{C3,C5}$ to slightly less positive values relative to rotamer XI that lacks this interaction (Figure 7C). This result contrasts with the effect of ψ on $^2J_{C3,C5}$ (Figures 4 and 7C) where the most positive $^2J_{C3,C5}$ value correlates with rotamer V in which the lone-pair orbitals on O1′ are anti to the C3−C4 and C4−C5 bonds. The effects of oxygen lone-pair orbitals on $^2J_{C3,C5}$ depend on whether the lone-pair resides on an oxygen atom attached to C3 or to C4.

3.6. Summary of $^2J_{CCH}$ Behavior in 2 and Saccharides in General. The results of studies on the effects of exocyclic C−O bond conformation on $^2J_{CCH}$ values in **2** are summarized in Scheme 11. Two types of C−O bond rotations pertain to C−C−H coupling pathways, those associated with the coupled carbon and those associated with the carbon bearing the coupled hydrogen. The latter C−O rotations exert the greater effect on $^2J_{CCH}$ values by a factor of 4−5. Thus, from the standpoint of conformational probes, the latter types of rotations, arising either from exocyclic C−O bonds of hydroxyl groups or C−O bonds involved in *O*-glycosidic linkages, are more likely to be interrogated successfully by $^2J_{CCH}$ values than the former.

In the preceding analysis, six $^2J_{CCH}$ were treated: $^2J_{C1',H2'}$, $^2J_{C2',H1'}$, $^2J_{C3,H4}$, $^2J_{C4,H3}$, $^2J_{C5,H4}$, and $^2J_{C4,H5}$. DFT calculations show that all but $^2J_{C2',H1'}$ have negative signs, regardless of C−O bond conformation at either carbon in the C−C−H coupling pathway. Application of the empirical projection rule of Pedersen and coworkers[28] gives signs that are generally consistent with the DFT calculations. The five DFT-calculated $^2J_{CCH}$ that have negative signs give projection sums of either −0.5 or 0, whereas the single $^2J_{CCH}$ having a positive sign ($^2J_{C2',H1'}$) gives a projection sum of +0.5. The former sums correlate with $^2J_{CCH}$ values ranging from −3 to −5 Hz, whereas a +0.5 sum correlates with $^2J_{CCH}$ values of ∼0 Hz (Figure S2,

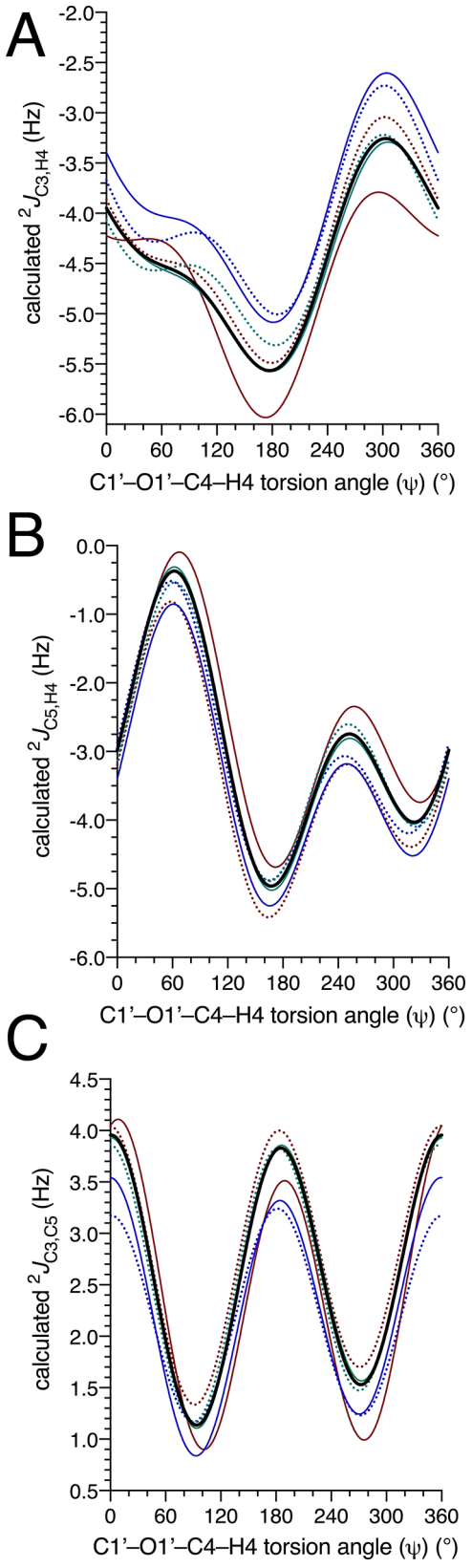

Figure 7. Effects of θ_1−θ_3 on the dependencies of $^2J_{C3,H4}$ (A), $^2J_{C5,H4}$ (B), and $^2J_{C3,C5}$ (C) on ψ in **2**. For each plot: black line, reference state; green dots, rotamer VII; green line, rotamer IX; blue dots, rotamer X; blue line, rotamer XII; red dots, rotamer XIII; red line, rotamer XV. For the definitions of rotamers and reference states, see Schemes S1−S3, Supporting Information.

https://doi.org/10.1021/acsomega.2c02793
ACS Omega 2022, 7, 23950−23966

Scheme 11. Summary of Oxygen Lone-Pair Effects on $^2J_{CCH}$ Values in Saccharides, Using $^2J_{C2',H1'}$ and $^2J_{C3,H4}$ in 2 as Examples[a]

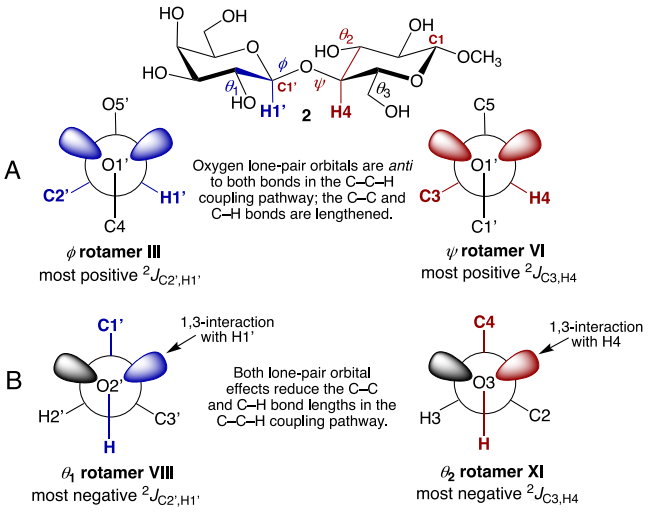

[a](A) Effect of the C−O bond rotation on the carbon bearing the coupled hydrogen. The φ (for $^2J_{C2',H1'}$) or ψ (for $^2J_{C3,H4}$) rotamers that orient both oxygen lone-pair orbitals *anti* to both bonds in the C−C−H coupling pathway correlate with the most positive *J*-values (these interactions are expected to lengthen both bonds). (B) Effect of C−O bond rotation on the coupled carbon. The value of θ_1 (for $^2J_{C2',H1'}$) and θ_2 (for $^2J_{C3,H4}$) rotamers in which the O−H bond is *anti* to the C−C bond in the coupling pathway, and one oxygen lone-pair orbital experiences a 1,3 interaction with the coupled hydrogen and correlates with the most negative *J*-values (both effects are expected to reduce the C−C and C−H bond lengths in the coupling pathway). See Schemes 8, 9, S1, and S2 for rotamers III, VI, VIII and XI, respectively.

Supporting Information). Inspection of the $^2J_{C2',H1'}$ curves in Figures 1C and 5B shows that both positive and negative signs are possible depending on ϕ and θ_1, giving an average value that is small in magnitude and positive in sign. The projection method only takes into account the configuration of the C−C−H coupling pathway and does not include contributions from C−O bond rotations at both carbons, which are significant.

3.7. Extensions to *O*-Glycosidic Linkages in Disaccharides 3−7. The preceding discussion of spin-coupling constants in **2** revealed several nonconventional ^1J and ^2J values that may be useful in *MA'AT* analyses of the *phi* and *psi* torsion angles in *O*-glycosidic linkages. Do the conclusions drawn from studies of **2** apply to β-(1→4) linkages involving modified residues and to (1→2) and (1→3) *O*-glycosidic linkages? To address these questions, calculations were conducted on five model disaccharides: methyl 2-acetamido-2-deoxy-β-D-glucopyranosyl-(1→4)-β-D-mannopyranoside (**3**), methyl 2-deoxy-β-D-arabino-hexopyranosyl-(1→4)-β-D-glucopyranoside (**4**), methyl α-D-mannopyranosyl-(1→3)-β-D-mannopyranoside (**5**), methyl α-D-mannopyranosyl-(1→2)-α-D-mannopyranoside (**6**), and methyl 2-acetamido-2-deoxy-β-D-glucopyranosyl-(1→2)-α-D-mannopyranoside (**7**) (Scheme 3). The behaviors of seven non-conventional *J*-couplings in **3**−**7** were compared to those of analogous *J*-couplings in **2**. The results are shown in Figures 8−10. For $^1J_{C1',C2'}$, the overall curve shape is conserved in **2**−**4** and **7**, in which the C1′−O1′ bond is equatorial and the O1′−CX bond (CX is the aglycone

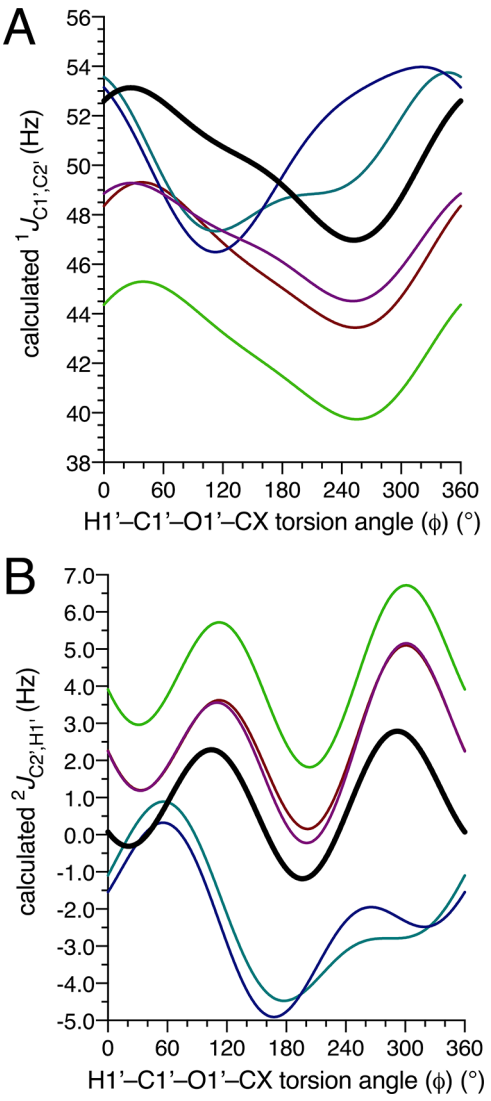

Figure 8. Calculated dependencies of $^1J_{C1',C2'}$ (A) and $^2J_{C2',H1'}$ (B) on the H1′−C1′−O1′−CX torsion angle (ϕ) in disaccharides **2**−**7**, where CX represents the aglycone carbon. Bold black curve, **2**. Purple curve, **3**. Lime green curve, **4**. Blue curve, **5**. Teal curve, **6**. Red curve, **7**.

carbon) is either axial (**7**) or equatorial (**2**−**4**) (Figure 8A). Absolute values of $^1J_{C1',C2'}$ decrease progressively in the order **2** > **3** ≈ **7** > **4**. The introduction of an *N*-acetyl side-chain on C2′ shifts $^1J_{C1',C2'}$ to smaller values, and removal of an electronegative substituent at C2′ further reduces $^1J_{C1',C2'}$. These curves differ appreciably from those for **5** and **6** that contain α-linkages in which the O1′−CX bond is either axial (**6**) or equatorial (**5**). The curve for **5** is an approximate mirror image of that for **2**, whereas that for **6** differs from that for **5** in the appearance of a local minimum near ϕ = 240°. The dynamic ranges of the curves for **3**−**7** are similar to that of the curve for **2**, supporting the contention that $^1J_{C1',C2'}$ should be a useful probe of ϕ in **3**−**7**. Separate equation parameterizations, however, will be required to treat $^1J_{C1',C2'}$ quantitatively in **2**−**7**.

The dependencies of $^2J_{C2',H1'}$ on ϕ in **2**−**4** and **7** are very similar, differing only in shifts along the *y*-axis (Figure 8B). $^2J_{C2',H1'}$ becomes increasingly more positive in the order **2** < **3** ≈ **7** < **4**. Curves for the α-linked disaccharides **5** and **6** are similar and are approximate mirror images of those for **2**−**4**

https://doi.org/10.1021/acsomega.2c02793
ACS Omega 2022, 7, 23950−23966

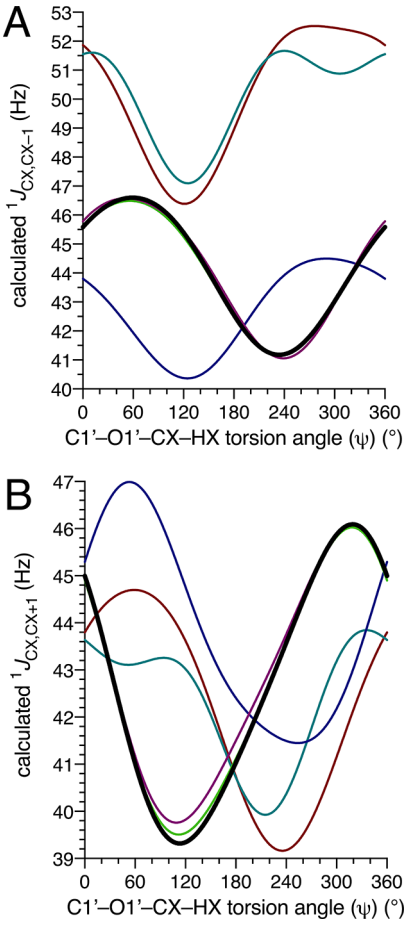

Figure 9. Calculated dependencies of $^1J_{CX,CX-1}$ (A) and $^1J_{CX,CX+1}$ (B) on the C1′−O1′−CX−HX torsion angle (ψ) in disaccharides **2**−**7**, where CX represents the aglycone carbon. For example, in **5**, $^1J_{CX,CX-1}$ = $^1J_{C3,C2}$ and $^1J_{CX,CX+1}$ = $^1J_{C3,C4}$. Bold black curve, **2**. Purple curve, **3**. Lime green curve, **4**. Blue curve, **5**. Teal curve, **6**. Red curve, **7**.

and **7**. $^2J_{C2',H1'}$ values are almost uniformly negative for the two α-linkages, whereas those for the β-linkages are almost uniformly positive, as observed for αMan and βGlc monosaccharides.[45] The dynamic ranges of all curves are similar, suggesting that $^2J_{C2',H1'}$ may be uniformly applicable in *MA'AT* analyses of ϕ. However, separate equation parameterizations will be required to apply $^2J_{C2',H1'}$ in *MA'AT* analyses.

One-bond $^{13}C-^{13}C$ spin-couplings sensitive to ψ are shown in Figure 9. The $^1J_{CX,CX-1}$ curves (Figure 9A) adopt similar shapes for **5**−**7**, whereas those for **2**−**4** overlap. The latter structures contain β-(1→4) linkages to aglycone residues bearing equatorial C−O bonds at C4 and C3. The side-chain structure at C2′ exerts little effect on this $^1J_{CC}$ nor does C−O bond orientation at the remote C2 (axial in **3** and equatorial in **2** and **4**). $^1J_{CX,CX-1}$ plots for **6** and **7** are similar and nearly overlap, and both are significantly shifted to larger $^1J_{CC}$ relative to the plot for **5**. Inspection of **6** and **7** shows that both contain an axial O1′−C2 bond and an axial C1−O1 bond, whereas corresponding bonds in **5** are equatorial and axial, respectively. The relative disposition of oxygen substituents appended to the coupled carbons over one bond (i.e., the dihedral angle subtended by the vicinal oxygen substituents; ∼180° in **6** and **7** and ∼−60° in **5**) is an important determinant of $^1J_{CC}$ values in saccharides.[43] The orientation of the C1′−O1′ bond, which is axial in **6** and equatorial in **7**, does not appear to influence

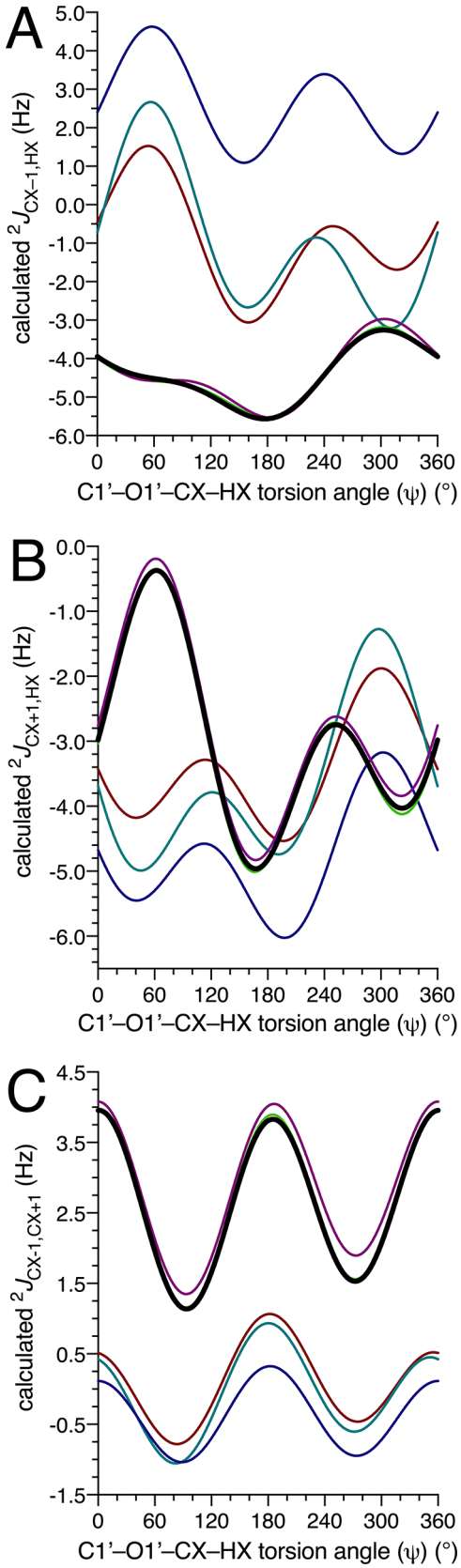

Figure 10. Calculated dependencies of $^2J_{CX-1,HX}$ (A), $^2J_{CX+1,HX}$ (B), and $^2J_{CX-1,CX+1}$ (C) on the C1′−O1′−CX−HX torsion angle (ψ) in disaccharides **2**−**7**, where CX represents the aglycone carbon. For example, in **5**, $^2J_{CX-1,HX}$ = $^2J_{C2,H3}$, $^2J_{CX+1,HX}$ = $^2J_{C4,H3}$, and $^2J_{CX-1,CX+1}$ = $^2J_{C2,C4}$. Bold black curve, **2**. Purple curve, **3**. Lime green curve, **4**. Blue curve, **5**. Teal curve, **6**. Red curve, **7**.

https://doi.org/10.1021/acsomega.2c02793
ACS Omega 2022, 7, 23950−23966

$^{1}J_{CX,CX-1}$ values appreciably. The dynamic range of the curve for **5** is somewhat smaller than that for **2**−**4** and **6**−**7**, which may render this $^{1}J_{CC}$ value less useful for *MA'AT* analyses of ψ in structures like **5**.

The dependencies of $^{1}J_{CX,CX+1}$ on ψ in **2**−**4** are virtually identical, producing overlapping curves (Figure 9B). The latter structures contain β-(1→4) linkages to aglycone residues bearing equatorial bonds at C4 and C5. The side-chain structure at C2′ exerts little effect on this $^{1}J_{CC}$ nor does C−O bond orientation at the remote C2 (axial in **3** and equatorial in **2** and **4**). The curves for **5**−**7**, which contain α anomeric linkages, have roughly similar shapes that are distinct from those for **2**−**4**. For **5**, the C−O bonds at C3 and C4 are both equatorial. In contrast, the C−O bonds at C2 and C3 are axial and equatorial, respectively, in **6** and **7**. These structural differences in the C_X−C_{X+1} coupling pathway may explain why the curves for **6** and **7** are similar and distinct from that for **5**.

Geminal ^{13}C−^{1}H and ^{13}C−^{13}C spin-couplings in **2**−**7** are shown in Figure 10, all of which are sensitive to ψ. The curve shapes for $^{2}J_{CX-1,HX}$ in **5**−**7** are conserved but are shifted along the *y*-axis, whereas the curves for **2**−**4** overlap and have shapes distinct from those found for **5**−**7** (Figure 10A). $^{2}J_{CX-1,HX}$ is positive or negative in sign in **6**−**7** depending on ψ, whereas $^{2}J_{CX-1,HX}$ is uniformly positive in **5**. In contrast, $^{2}J_{CX-1,HX}$ values in **2**−**4** are strongly negative. These observations are consistent with predictions based on the projection rule,[28] where a projection of 0 is associated with the C3−C4−H4 pathways in **2**−**4**, and a projection of 1.5 is associated with the C2−C3−H3 pathway in **5**, yielding predicted $^{2}J_{CCH}$ values of ∼−3 and ∼+5 Hz, respectively (see Figure S2 in Supporting Information), in qualitative agreement with the DFT results. The dynamic ranges of $^{2}J_{CX-1,HX}$ in **5**−**7** may render them more useful for *MA'AT* analysis of ψ than those of $^{2}J_{CX-1,HX}$ in **2**−**4**. Similar behavior is observed for $^{2}J_{CX+1,HX}$ (Figure 10B) in that curves of similar shape are observed for **5**−**7** but are shifted along the *y*-axis, whereas the curves for **2**−**4** overlap and have shapes distinct from those for **5**−**7**. $^{2}J_{CX+1,HX}$ values in **2**−**7** are negative in sign and all exhibit a dynamic range suitable for *MA'AT* analysis of ψ.

The geminal $^{2}J_{CX-1,CX+1}$ shows a remarkable consistency in its dependency on ψ (Figure 10C), regardless of the location of the pathway in the pyranosyl ring. Two sets of curves are observed. One set includes $^{2}J_{CX-1,CX+1}$ values that have uniformly positive signs and is associated with pathways in which the oxygens on the terminal coupled carbons are both equatorial (structures **2**−**4**). The second set includes $^{2}J_{CX-1,CX+1}$ values with signs near zero and is associated with pathways in which the oxygens on the terminal coupled carbons are axial and equatorial (structures **5**−**7**). C−O Bond orientation (axial vs equatorial) at the intervening carbon in these C−C−C pathways appears to exert a minimal effect on $^{2}J_{CCC}$. The dynamic range of pathways having two equatorial terminal oxygens is larger than that of pathways having an axial-equatorial arrangement, leading to the expectation that $^{2}J_{CX-1,CX+1}$ values in the former will be more robust *MA'AT* constraints on ψ than $^{2}J_{CX-1,CX+1}$ values in the latter.

3.8. Behavior of $^{4}J_{H1',H4}$ in Disaccharides 2, 5, and 6.

Trans-*O*-Glycoside four-bond spin-coupling between H1′ and HX (HX is the hydrogen attached to the aglycone carbon) is not expected to be a useful probe in *MA'AT* analyses of *O*-glycosidic linkages. Nevertheless, it was investigated to gain a better understanding of its dependence on linkage conformation. Plots of calculated $^{4}J_{H1',H4}$ in **2** as a function of ϕ and ψ are shown in Figure 11. $^{4}J_{H1',H4}$ values are small in magnitude

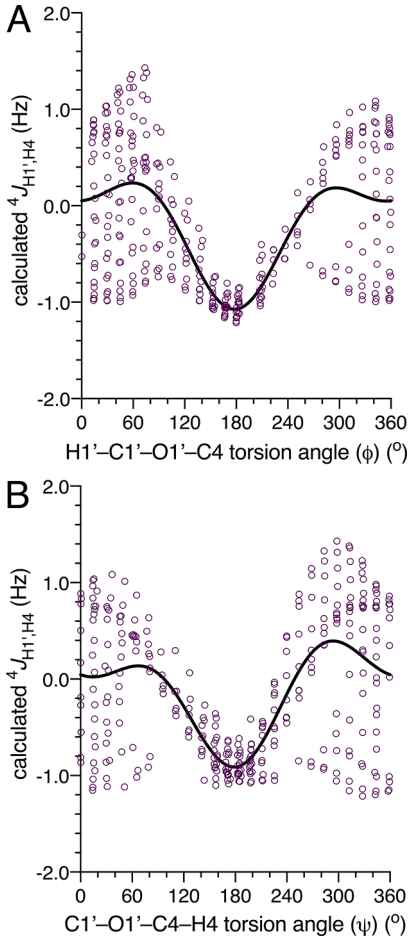

Figure 11. Calculated dependencies of $^{4}J_{H1',H4}$ on (A) H1′−C1′−O1′−C4 (ϕ) and (B) C1′−O1′−C4−H4 (ψ) torsion angles in **2**. In each plot, the black curve represents the best fit of the data. Point scatter at discrete values of ϕ in (A) and ψ in (B) indicate the extent to which ψ and ϕ, respectively, affect the calculated coupling.

and have a dynamic range of ∼2 Hz. $^{4}J_{H1',H4}$ is equally sensitive to ϕ and ψ, as indicated by the data scatter at discrete values of ϕ in Figure 11A and ψ in Figure 11B. This scatter reaches a minimum at a ϕ/ψ combination of 180/180°, that is, when the five atoms in the H1′−C1′−O1′−C4−H4 coupling pathway are coplanar and adopt a W-shaped arrangement.[40,46] Recent *MA'AT* analyses of **2**[10] have yielded mean values of ϕ and ψ of 28° and −8°, respectively, where secondary effects on $^{4}J_{H1',H4}$ are significant, thereby rendering $^{4}J_{H1',H4}$ useless as an independent probe of either torsion angle. However, $^{4}J_{H1',H4}$ could play a confirmatory role if ϕ and ψ in a given linkage were determined from *MA'AT* analyses of other *J*-couplings. In this case, complicating secondary effects are reduced, and $^{4}J_{H1',H4}$ can be used as an ancillary test of the conformational assignment. This scenario is illustrated in Figure 12 for $^{4}J_{H1',H4}$ in **2**. Using *MA'AT*-determined mean values of ϕ and ψ, a $^{4}J_{H1',H4}$ of ∼0.9 Hz should be observed, a value with a small uncertainty based on the imposed limited scatter from secondary effects. In practice, however, while coupling trends predicted by DFT are probably reliable, it remains to be established whether $^{4}J_{H1',H4}$ values calculated by DFT are

https://doi.org/10.1021/acsomega.2c02793
ACS Omega 2022, 7, 23950−23966

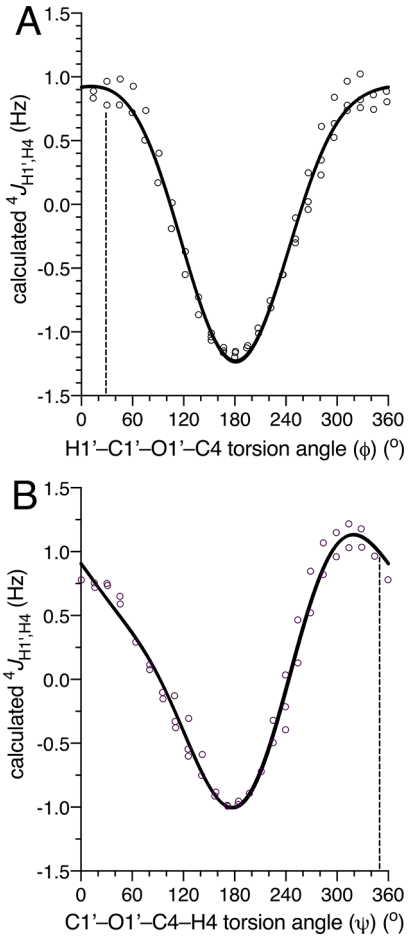

Figure 12. Calculated dependencies of $^4J_{H1',H4}$ on (A) H1′−C1′−O1′−C4 (ϕ) and (B) C1′−O1′−C4−H4 (ψ) torsion angles in **2**. In each plot, the black curve represents the best fit of the data. Point scatter at discrete values of ϕ in (A) and ψ in (B) indicate the extent to which ψ and ϕ, respectively, affect the calculated coupling, using restricted ranges of ψ (−30 to 15°) and ϕ (15−45°). The vertical dashed line in each plot identifies the mean value of ϕ (28°) and ψ (−8°) in **2** determined from prior *MA'AT* analysis.[10]

accurate; that is, the curves in Figures 11 and 12 may need to be shifted on the *y*-axes to bring calculated values in line with experiment.

The behavior of $^4J_{H1',H4}$ in **2** as a function of ϕ and ψ (Figure 11) appears to be independent of the type of *O*-glycosidic linkage. In **2**, the C1′−O1′ and C4−O1′ bonds are both equatorial. In **5**, the C1′−O1′ bond is axial and the C3−O1′ bond is equatorial, and in **6**, the C1′−O1′ and C2−O1′ bonds are both axial. Plots similar to those shown in Figure 11 for **2** are shown in Figures S3 and S4 for **5** and **6**, respectively (see Supporting Information). The latter plots are very similar to those found for **2** with respect to the location of the minimum, dynamic range, the absolute values of the calculated *J*-couplings, and the nature of the secondary dependencies. Thus, the conclusions drawn regarding the ancillary role of $^4J_{H1',H4}$ in evaluating ϕ and ψ in **2** also apply to the corresponding trans-glycosidic $^4J_{HH}$ values in **5** and **6** and probably to other types of *O*-glycosidic linkages.

3.9. DFT-Parameterized Spin-Coupling Equations for Structures 2−7. Plots of *J*-couplings in structures **2**−**7** as a function of either the *phi* (ϕ) or *psi* (ψ) *O*-glycosidic torsion angles (Figures 1−12) were parameterized and are found in the Supporting Information (eqs S1−S105). The curves were fit to the following modified Karplus-like equation (eq 1) using R.

$$ {}^{n}J_{x,y}(\mathrm{Hz}) = k + a\cos\theta + b\sin\theta + c\cos 2\theta + d\sin 2\theta + e\cos 3\theta + f\sin 3\theta \quad (1) $$

This generalized form of the Karplus-like equation was first described by Pachler.[47] He proposed the use of this trigonometric function to account for asymmetry in the Karplus curve caused by substitution of a hydrogen atom in the coupling pathway. This trigonometric polynomial form was adopted because it provides the best parameterization to the DFT data with the smallest number of terms. This form of the equation is also amenable to simple integration, making it compatible with *MA'AT* analysis[9−12] for modeling torsional populations in solution.

4. CONCLUSIONS

MA'AT modeling of conformational equilibria and dynamics of saccharides depends in part on reliable equations that relate specific spin-coupling constants to molecular torsion angles.[9−12] It has been customary to use ^3J values (e.g., $^3J_{HH}$, $^3J_{CH}$, and $^3J_{CC}$) in this modeling for three reasons: (1) these *J*-couplings typically exhibit strong dependencies on molecular torsion angles (i.e., have large dynamic ranges); (2) they are less prone to secondary structural effects, especially those associated with the rotation of proximal bonds bearing electronegative substituents (e.g., C−O bonds); and (3) the conformational dependencies of other types of spin-coupling constants (e.g., ^1J, ^2J and ^4J) are less well understood. Saccharides like other types of molecules are rich in ^1J, ^2J, and ^3J values involving carbon and hydrogen as coupled nuclei. However, restricting *MA'AT* analyses to ^3J values eliminates nearly 60% of the available *J*-couplings in an aldohexopyranosyl ring, excluding those involving hydroxyl hydrogens.[40] For unimodal modeling, access to 3−4 redundant *J*-couplings (i.e., those sensitive to the same molecular torsion angle) is sufficient for successful *MA'AT* modeling.[9−12] For multimodal modeling, however, significantly more redundant *J*-couplings are needed, rendering the use of ^1J and/or ^2J values important to wider applications of the method. In the absence of using ^1J and/or ^2J values, additional types of NMR parameters (e.g., residual dipolar couplings or nuclear Overhauser effects) might also enable multimodal modeling.

This study investigated a group of nonconventional *J*-couplings (mainly ^2J values) that are not commonly used in conformational analysis of the *O*-glycosidic linkages of oligosaccharides. Thirteen *J*-couplings in six different types of *O*-glycosidic linkages were investigated. The results show that seven of these *J*-couplings may prove useful in *MA'AT* modeling of either ϕ or ψ under certain conditions, regardless of the type of *O*-glycosidic linkage (e.g., 1→2 vs 1→3 linkages; α vs β linkages). The latter conditions are likely to include prior knowledge of the conformational behaviors of exocyclic C−O bonds proximal to the coupling pathway. This knowledge would reduce the negative impacts of secondary effects on *MA'AT* modeling of *O*-glycosidic linkage conformation when nonconventional *J*-couplings are used as conformational constraints. This knowledge would also improve, although more modestly, the reliability of *MA'AT* modeling of ϕ and ψ based on conventional ^3J values.

https://doi.org/10.1021/acsomega.2c02793
ACS Omega 2022, 7, 23950−23966

Experimental studies of the conformational properties of exocyclic C−O bonds in solution have been reported,[48−53] and MD simulations provide additional information even though current force fields are not parameterized to provide this information quantitatively. MD simulations of exocyclic hydroxyl C−O bonds not participating in hydrogen bonding show three idealized staggered rotamers to be most stable, although often in different populations. Whether this behavior replicates that found in solution accurately awaits more rigorous experimental study.

While the present study investigated new nonconventional *J*-couplings of importance to *MA'AT* modeling of *O*-glycosidic linkage conformation and dynamics, nonconventional spin-couplings may also prove useful in *MA'AT* modeling of other conformational properties of saccharides in solution. Unlike *O*-glycosidic linkages that often adopt single-state conformations about ϕ and ψ, multi-state conformational equilibria may pertain to other conformational behaviors (e.g., exocyclic hydroxyl and hydroxymethyl group conformations). Multi-state modeling of hydroxyl group conformations by *MA'AT* analysis would be enabled by use of nonconventional *J*-couplings like those discussed in this report. This modeling not only would advance our current rudimentary understanding of exocyclic C−O bond conformational behavior in solution but would also improve *MA'AT* modeling in general by reducing or eliminating secondary effects displayed by some redundant *J*-couplings used in *MA'AT* analyses.

■ ASSOCIATED CONTENT

Supporting Information

The Supporting Information is available free of charge at https://pubs.acs.org/doi/10.1021/acsomega.2c02793.

Three idealized staggered rotamers VII−IX about the C2′−O2′ bond (θ_1) in **2**; three idealized staggered rotamers X−XII about the C3−O3 bond (θ_2) in **2**; three idealized staggered rotamers XIII−XV about the C5−C6 bond (θ_3) in **2**; plots of calculated $^1J_{C1',H1'}$, $^2J_{C1',H2'}$, $^1J_{C4,H4}$, $^2J_{C4,H3}$, and $^2J_{C4,H5}$ values as a function of either the H1′−C1′−O1′−C4 (ϕ) or the C1′−O1′−C4−H4 (ψ) torsion angle for different values of θ_1, θ_2, and θ_3 in **2**; and a discussion of these plots; torsion angle constraints in DFT calculations of **3**−**7**; plot of projection sums used to predict the magnitudes and signs of $^2J_{CCH}$ values in saccharides; plots of calculated $^4J_{H1',H3}$ in **5** as functions of ϕ and ψ; plots of calculated $^4J_{H1',H2}$ in **6** as functions of ϕ and ψ; DFT-parameterized spin-coupling equations [S1]−[S105]; and representative Cartesian coordinates for **2**−**7** (PDF)

■ AUTHOR INFORMATION

Corresponding Author

Anthony S. Serianni − *Department of Chemistry and Biochemistry, University of Notre Dame, Notre Dame, Indiana 46556-5670, United States;* orcid.org/0000-0001-6114-1446; Email: aseriann@nd.edu

Authors

Reagan J. Meredith − *Department of Chemistry and Biochemistry, University of Notre Dame, Notre Dame, Indiana 46556-5670, United States;* orcid.org/0000-0001-7330-3190

Ian Carmichael − *Radiation Laboratory, University of Notre Dame, Notre Dame, Indiana 46556-5670, United States*

Complete contact information is available at: https://pubs.acs.org/10.1021/acsomega.2c02793

Notes

The authors declare no competing financial interest.

■ ACKNOWLEDGMENTS

This work was supported by the National Science Foundation (CHE 1707660 and CHE 2002625 to A. S.) and by Omicron Biochemicals, Inc., South Bend, IN. The Notre Dame Radiation Laboratory is supported by the Department of Energy Office of Science, Office of Basic Energy Sciences, under Award Number DE-FC02-04ER15533. This is document number NDRL 5326.

■ REFERENCES

(1) Yu, Y.; Delbianco, M. Conformational Studies of Oligosaccharides. *Chem. - Eur. J.* **2020**, *26*, 9814−9825.

(2) Zhang, Y.; Yamaguchi, T.; Kato, K. New NMR Tools for Characterizing the Dynamic Conformations and Interactions of Oligosaccharides. *Chem. Lett.* **2013**, *42*, 1455−1462.

(3) Watanabe, T.; Yagi, H.; Yanaka, S.; Yamaguchi, T.; Kato, K. Comprehensive Characterization of Oligosaccharide Conformational Ensembles with Conformer Classification by Free-energy Landscape via Reproductive Kernel Hilbert Space. *Phys. Chem. Chem. Phys.* **2021**, *23*, 9753−9760.

(4) Woods, R. J. Predicting the Structures of Glycans, Glycoproteins, and Their Complexes. *Chem. Rev.* **2018**, *118*, 8005−8024.

(5) Johnson, Q.; Lindsay, R.; Petridis, L.; Shen, T. Investigation of Carbohydrate Recognition via Computer Simulation. *Molecules* **2015**, *20*, 7700−7718.

(6) Plazinska, A.; Plazinski, W. Comparison of Carbohydrate Force Fields in Molecular Dynamics Simulations of Protein-Carbohydrate Complexes. *J. Chem. Theory Comput.* **2021**, *17*, 2575−2585.

(7) Park, S.-J.; Lee, J.; Qi, Y.; Kern, N. R.; Lee, H. S.; Jo, S.; Joung, I.; Joo, K.; Lee, J.; Im, W. CHARMM-GUI Glycan Modeler for Modeling and Simulation of Carbohydrates and Glycoconjugates. *Glycobiology* **2019**, *29*, 320−331.

(8) Yang, M.; MacKerell, A. D., Jr. Conformational Sampling of Oligosaccharides Using Hamiltonian Replica Exchange with Two-Dimensional Dihedral Biasing Potentials and the Weighted Histogram Analysis Method (WHAM). *J. Chem. Theory Comput.* **2015**, *11*, 788−799.

(9) Turney, T.; Pan, Q.; Sernau, L.; Carmichael, I.; Zhang, W.; Wang, X.; Woods, R. J.; Serianni, A. S. *O*-Acetyl Side-Chains in Monosaccharides: Redundant NMR Spin-Couplings and Statistical Models for Acetate Ester Conformational Analysis. *J. Phys. Chem. B* **2017**, *121*, 66−77.

(10) Zhang, W.; Turney, T.; Meredith, R.; Pan, Q.; Sernau, L.; Wang, X.; Hu, X.; Woods, R. J.; Carmichael, I.; Serianni, A. S. Conformational Populations of β-(1→4) *O*-Glycosidic Linkages Using Redundant NMR *J*-Couplings and Circular Statistics. *J. Phys. Chem. B* **2017**, *121*, 3042−3058.

(11) Zhang, W.; Meredith, R.; Yoon, M.-K.; Wang, X.; Woods, R. J.; Carmichael, I.; Serianni, A. S. Synthesis and *O*-Glycosidic Linkage Conformational Analysis of ^{13}C-Labeled Oligosaccharide Fragments of an Antifreeze Glycolipid. *J. Org. Chem.* **2019**, *84*, 1706−1724.

(12) Zhang, W.; Meredith, R.; Pan, Q.; Wang, X.; Woods, R. J.; Carmichael, I.; Serianni, A. S. Use of Circular Statistics To Model αMan-(1→2)-αMan and αMan-(1→3)α/βMan *O*-Glycosidic Linkage Conformation in ^{13}C-Labeled Disaccharides and High-Mannose Oligosaccharides. *Biochemistry* **2019**, *58*, 546−560.

(13) Thibaudeau, C.; Stenutz, R.; Hertz, B.; Klepach, T.; Zhao, S.; Wu, Q.; Carmichael, I.; Serianni, A. S. Correlated C−C and C−O Bond Conformations in Saccharide Hydroxymethyl Groups: Param-

eterization and Application of Redundant ^{1}H-^{1}H, ^{13}C-^{1}H and ^{13}C-^{13}C NMR *J*-couplings. *J. Am. Chem. Soc.* **2004**, *126*, 15668−15685.
(14) Bose, B.; Zhao, S.; Stenutz, R.; Cloran, F.; Bondo, P. B.; Bondo, G.; Hertz, B.; Carmichael, I.; Serianni, A. S. Three-Bond C−O−C−C Spin-Coupling Constants in Carbohydrates: Development of a Karplus Relationship. *J. Am. Chem. Soc.* **1998**, *120*, 11158−11173.
(15) Meredith, R. J.; Woods, R. J.; Carmichael, I.; Serianni, A. S. Reconciling *MA′AT* and Molecular Dynamics Models of Linkage Conformation in Oligosaccharides. *Phys. Chem. Chem. Phys.* **2020**, *22*, 14454−14457.
(16) Frisch, M. J.; et al. *Gaussian09, Revision D*; Gaussian Inc.: Wallingford, CT, 2009.
(17) Becke, A. D. Density-Functional Thermochemistry. III. The Role of Exact Exchange. *J. Chem. Phys.* **1993**, *98*, 5648−5652.
(18) Becke, A. D. New Mixing of Hartree-Fock and Local Density-Functional Theories. *J. Chem. Phys.* **1993**, *98*, 1372−1377.
(19) Hehre, W. J.; Ditchfield, R.; Pople, J. A. Self-Consistent Molecular Orbital Methods. XII. Further Extensions of Gaussian-Type Basis Sets for Use in Molecular Orbital Studies of Organic Molecules. *J. Chem. Phys.* **1972**, *56*, 2257−2261.
(20) Cancès, E.; Mennucci, B.; Tomasi, J. A New Integral Equation Formalism for the Polarizable Continuum Model: Theoretical Background and Applications To Isotropic and Anisotropic Dielectrics. *J. Chem. Phys.* **1997**, *107*, 3032−3041.
(21) Cammi, R.; Mennucci, B.; Tomasi, J. Fast Evaluation of Geometries and Properties of Excited Molecules in Solution: A Tamm-Dancoff Model with Application to 4-Dimethyl-amino-benzonitrile. *J. Phys. Chem. A* **2000**, *104*, 5631−5637.
(22) Sychrovský, V.; Gräfenstein, J.; Cremer, D. Nuclear Magnetic Resonance Spin−Spin Coupling Constants from Coupled Perturbed Density Functional Theory. *J. Chem. Phys.* **2000**, *113*, 3530−3547.
(23) Helgaker, T.; Watson, M.; Handy, N. C. Analytical Calculation of Nuclear Magnetic Resonance Indirect Spin−Spin Coupling Constants at the Generalized Gradient Approximation and Hybrid Levels of Density-Functional Theory. *J. Chem. Phys.* **2000**, *113*, 9402−9409.
(24) Barone, V.; Peralta, J. E.; Contreras, R. H.; Snyder, J. P. DFT Calculation of NMR J_{FF} Spin Spin Coupling Constants in Fluorinated Pyridines. *J. Phys. Chem. A* **2002**, *106*, 5607−5612.
(25) Klepach, T.; Zhao, H.; Hu, X.; Zhang, W.; Stenutz, R.; Hadad, M. J.; Carmichael, I.; Serianni, A. S. Informing Saccharide Structural NMR Studies with Density Functional Theory Calculations. In *Glycoinformatics: Methods in Molecular Biology*; Lütteke, T., Frank, M., Eds.; Springer: New York, 2015, pp 289−331.
(26) Stenutz, R.; Carmichael, I.; Widmalm, G.; Serianni, A. S. Hydroxymethyl Group Conformation in Saccharides: Structural Dependencies of $^{2}J_{HH}$, $^{3}J_{HH}$ and $^{1}J_{CH}$ Spin-Spin Coupling Constants. *J. Org. Chem.* **2002**, *67*, 949−958.
(27) Bose-Basu, B.; Klepach, T.; Bondo, G.; Bondo, P. B.; Zhang, W.; Carmichael, I.; Serianni, A. S. ^{13}C-^{13}C NMR Spin-Spin Coupling Constants in Saccharides: Structural Correlations Involving All Carbons In Aldopyranosyl Rings. *J. Org. Chem.* **2007**, *72*, 7511−7522.
(28) Pedersen, C.; Bock, K.; Popoff, T.; Theander, O.; Nørskov, L.; Schroll, G. Two- and Three-bond ^{13}C-^{1}H Couplings in Some Carbohydrates. *Acta Chem. Scand.* **1977**, *31b*, 354−358.
(29) Serianni, A. S.; Podlasek, C. A. ^{13}C-^{1}H Spin-coupling Constants in Carbohydrates: Magnitude and Sign Determinations via 2D NMR Methods. *Carbohydr. Res.* **1994**, *259*, 277−282.
(30) Church, T.; Carmichael, I.; Serianni, A. S. Two-bond ^{13}C-^{13}C Spin-coupling Constants in Carbohydrates: Effect of Structure on Coupling Magnitude and Sign. *Carbohydr. Res.* **1996**, *280*, 177−186.
(31) Serianni, A. S.; Bondo, P. B.; Zajicek, J. Verification of the Projection Resultant Method for Two-bond ^{13}C-^{13}C Coupling Sign Determinations in Carbohydrates. *J. Magn. Reson.* **1996**, *112*, 69−74.
(32) Zhao, S.; Bondo, G.; Zajicek, J.; Serianni, A. S. Two-bond ^{13}C-^{13}C Spin-coupling Constants in Carbohydrates: New Measurements of Coupling Signs. *Carbohydr. Res.* **1998**, *309*, 145−152.
(33) Akaike, H. New Look at the Statistical Model Identification. *IEEE Trans. Autom. Control* **1974**, *19*, 716−723.
(34) Freymann, R.; Gueron, J. Absorption Spectra in the Near Infra Red of Systems Constituted of Chlorhydric Gas and an Organic Oxygen Solvant. *C. R. Acad. Sci.* **1937**, *205*, 859−861.
(35) Wolfe, S.; Pinto, B. M.; Varma, V.; Leung, R. Y. N. The Perlin Effect: Bond Lengths, Bond Strengths, and the Origins of Stereoelectronic Effects Upon One-Bond C−H Coupling Constants. *Can. J. Chem.* **1990**, *68*, 1051−1062.
(36) Juaristi, E.; Cuevas, G. *The Anomeric Effect*; CRC Press: Boca Raton, 1995, pp 95−111.
(37) Clauss, A. D.; Nelsen, S. F.; Ayoub, M.; Moore, J. W.; Landis, C. R.; Weinhold, F. Rabbit-ears Hybrids, VSEPR Sterics, and Other Orbital Anachronisms. *Chem. Educ. Res. Pract.* **2014**, *15*, 417−434.
(38) Stewart, J. J. P. An Examination of the Nature of Localized Molecular Orbitals and Their Value In Understanding Various Phenomena That Occur In Organic Chemistry. *J. Mol. Model.* **2019**, *25*, 7−23.
(39) Klepach, T. E.; Carmichael, I.; Serianni, A. S. Geminal $^{2}J_{CCH}$ Spin-Spin Coupling Constants as Probes of the ϕ Glycosidic Torsion Angle in Oligosaccharides. *J. Am. Chem. Soc.* **2005**, *127*, 9781−9793.
(40) Hadad, M. J.; Zhang, W.; Turney, T.; Sernau, L.; Wang, W.; Woods, R. J.; Incandela, A.; Surjancev, I.; Wang, A.; Yoon, M.-K.; Coscia, A.; Euell, C.; Meredith, R.; Carmichael, I.; Serianni, A. S. NMR Spin-Couplings in Saccharides: Relationships Between Structure, Conformation and the Magnitudes of J_{HH}, J_{CH} and J_{CC} Values. In *New Developments in NMR 10: NMR in Glycoscience and Glycotechnology*; Peters, T., Kato, K., Eds.; Royal Society of Chemistry, 2017, pp 20−100.
(41) Otter, A.; Bundle, D. R. Long-range ^{4}J and ^{5}J, Including Interglycosidic Correlations in Gradient-enhanced Homonuclear COSY Experiments of Oligosaccharides. *J. Magn. Reson., Ser. B* **1995**, *109*, 194−201.
(42) Sheng, S.; Cherniak, R.; van Halbeek, H. A ^{1}H NMR Spectroscopic Approach to the Unambiguous Determination of Glycosyl Linkage Positions in Oligosaccharides. *Anal. Biochem.* **1998**, *256*, 63−66.
(43) Carmichael, I.; Chipman, D. M.; Podlasek, C. A.; Serianni, A. S. Torsional Effects on the One-Bond ^{13}C-^{13}C Spin Coupling Constant in Ethylene Glycol: Insights Into the Behavior of $^{1}J_{CC}$ in Carbohydrates. *J. Am. Chem. Soc.* **1993**, *115*, 10863−10870.
(44) Zhang, W.; Yoon, M.-K.; Meredith, R. J.; Zajicek, J.; Oliver, A. G.; Hadad, M.; Frey, M. H.; Carmichael, I.; Serianni, A. S. ^{13}C−^{13}C Spin-Coupling Constants in Crystalline ^{13}C-Labeled Saccharides: Conformational Effects Interrogated by Solid-State ^{13}C NMR Spectroscopy. *Phys. Chem. Chem. Phys.* **2019**, *21*, 23576−23588.
(45) Podlasek, C. A.; Wu, J.; Stripe, W. A.; Bondo, P. B.; Serianni, A. S. [^{13}C]Enriched Methyl Aldopyranosides: Structural Interpretations of ^{13}C-^{1}H Spin-Coupling Constants and ^{1}H Chemical Shifts. *J. Am. Chem. Soc.* **1995**, *117*, 8635−8644.
(46) Barfield, M.; Dean, A. M.; Fallick, C. J.; Spear, R. J.; Sternhell, S.; Westerman, P. W. Conformational Dependence and Mechanisms For Long-range Hydrogen-Hydrogen Coupling Constants Over Four Bonds. *J. Am. Chem. Soc.* **1975**, *97*, 1482−1492.
(47) Pachler, K. G. R. Extended Hückel Theory MO Calculations of Proton-Proton Coupling Constants−II: The Effect of Substituents on Vicinal Couplings in Monosubstituted Ethanes. *Tetrahedron* **1971**, *27*, 187−199.
(48) Kindahl, L.; Sandström, C.; Norberg, T.; Kenne, L. ^{1}H NMR Studies of Hydroxy Protons of Asn- and Ser-Linked Disaccharides in Aqueous Solution. *J. Carbohydr. Chem.* **2000**, *19*, 1291−1303.
(49) Poppe, L.; van Halbeek, H. NMR Spectroscopy of Hydroxyl Protons in Supercooled Carbohydrates. *Nat. Struct. Biol.* **1994**, *1*, 215−216.
(50) Adams, B.; Lerner, L. Observation of Hydroxyl Protons of Sucrose in Aqueous Solution: No Evidence for Persistent Intramolecular Hydrogen Bonds. *J. Am. Chem. Soc.* **1992**, *114*, 4827−4829.
(51) Sandström, C.; Baumann, H.; Kenne, L. NMR Spectroscopy of Hydroxy Protons of 3,4-Disubstituted Methyl α-D-Galactopyranosides in Aqueous Solution. *J. Chem. Soc., Perkin Trans.* **1988**, *2*, 809−816.

https://doi.org/10.1021/acsomega.2c02793
ACS Omega 2022, 7, 23950−23966

(52) Batta, G.; Kövér, K. E. Heteronuclear Coupling Constants of Hydroxyl Protons in a Water Solution of Oligosaccharides: Trehalose and Sucrose. *Carbohydr. Res.* **1999**, *320*, 267−272.
(53) Zhao, H.; Pan, Q.; Zhang, W.; Carmichael, I.; Serianni, A. S. DFT and NMR Studies of $^{2}J_{COH}$, $^{3}J_{HCOH}$, and $^{3}J_{CCOH}$ Spin-Couplings in Saccharides: C−O Torsional Bias and H-Bonding in Aqueous Solution. *J. Org. Chem.* **2007**, *72*, 7071−7082.

https://doi.org/10.1021/acsomega.2c02793
ACS Omega 2022, 7, 23950−23966